

1 **MitoChime: A Machine Learning Pipeline for**
2 **Detecting PCR-Induced Chimeras in**
3 **Mitochondrial Illumina Reads**

4 A Special Project Proposal
5 Presented to
6 the Faculty of the Division of Physical Sciences and Mathematics
7 College of Arts and Sciences
8 University of the Philippines Visayas
9 Miagao, Iloilo

10 In Partial Fulfillment
11 of the Requirements for the Degree of
12 Bachelor of Science in Computer Science

13 by

14 Duranne Duran
15 Yvonne Lin
16 Daniella Pailden

17 Adviser
18 Francis D. Dimzon, Ph.D.

19 February 7, 2026

Abstract

21 Next-generation sequencing (NGS) platforms have advanced research but re-
22 main susceptible to artifacts such as PCR-induced chimeras that compromise
23 mitochondrial genome assembly. These artificial hybrid sequences are prob-
24 lematic for small, circular, and repetitive mitochondrial genomes, where they
25 can generate fragmented contigs and false junctions. Existing detection tools,
26 such as UCHIME, are optimized for amplicon-based microbial community ana-
27 lysis and depend on reference databases or abundance assumptions unsuitable
28 for organellar assembly. To address this gap, this study presents MitoChime,
29 a machine learning pipeline for detecting PCR-induced chimeric reads in *Sar-*
30 *dinella lemuru* Illumina paired-end data without relying on external reference
31 databases.

32 Using simulated datasets containing clean and chimeric reads, a feature
33 set was extracted, combining alignment-based metrics (e.g., supplementary
34 alignments, soft-clipping) with sequence-derived statistics (e.g., k-mer com-
35 position, microhomology). A comparative evaluation of supervised learning
36 models identified tree-based ensembles CatBoost and Gradient Boosting as top
37 performers, achieving an F1-score of 0.77 and an ROC-AUC of 0.84 on held-
38 out test data. Feature importance analysis highlighted soft-clipping and k-mer
39 compositional shifts as the strongest predictors of chimerism, whereas micro-
40 homology contributed minimally. Integrating MitoChime as a pre-assembly
41 step can aid in streamlining mitochondrial reconstruction pipelines.

42 **Keywords:** Chimera detection, Mitochondrial genome,
Assembly, Machine learning

⁴³ **Contents**

⁴⁴	1 Introduction	1
⁴⁵	1.1 Overview	1
⁴⁶	1.2 Problem Statement	3
⁴⁷	1.3 Research Objectives	3
⁴⁸	1.3.1 General Objective	3
⁴⁹	1.3.2 Specific Objectives	4
⁵⁰	1.4 Scope and Limitations of the Research	4
⁵¹	1.5 Significance of the Research	6
⁵²	2 Review of Related Literature	7
⁵³	2.1 The Mitochondrial Genome	7
⁵⁴	2.1.1 Mitochondrial Genome Assembly	8

55	2.2 PCR Amplification and Chimera Formation	9
56	2.3 Existing Traditional Approaches for Chimera Detection	10
57	2.3.1 UCHIME	11
58	2.3.2 UCHIME2	12
59	2.3.3 CATch	13
60	2.3.4 ChimPipe	14
61	2.4 Machine Learning Approaches for Chimera and Sequence Quality	
62	Detection	15
63	2.4.1 Feature-Based Representations of Genomic Sequences . . .	15
64	2.5 Synthesis of Chimera Detection Approaches	16
65	3 Research Methodology	19
66	3.1 Research Activities	19
67	3.1.1 Data Collection	20
68	3.1.2 Feature Extraction Pipeline	23
69	3.1.3 Machine Learning Model Development	26
70	3.1.4 Model Benchmarking, Hyperparameter Optimization, and	
71	Evaluation	27
72	3.1.5 Feature Importance, Feature Selection, and Interpretation	29

73	3.1.6 Validation and Testing	31
74	3.1.7 Documentation	32
75	3.2 Calendar of Activities	32
76	4 Results and Discussion	34
77	4.1 Descriptive Analysis of Features	35
78	4.1.1 Summary Statistics Per Class	35
79	4.1.2 Correlation Analysis of Extracted Features	40
80	4.2 Baseline Classification Performance	41
81	4.3 Effect of Hyperparameter Tuning	43
82	4.4 Detailed Evaluation of Representative Models	45
83	4.4.1 Confusion Matrices and Error Patterns	45
84	4.4.2 ROC and Precision–Recall Curves	47
85	4.5 Feature Importance	48
86	4.5.1 Permutation Importance of Individual Features	48
87	4.5.2 Feature Family Importance	50
88	4.6 Feature Selection	52
89	4.6.1 Cumulative Importance Curve	53

90	4.6.2 Performance Comparison Across Feature Sets	53
91	4.6.3 Interpretation and Final Feature Set Choice	55
92	4.7 Summary of Findings	55
93	A Complete Per-Class Summary Statistics	57
94	B Boxplots for All Numeric Features by Feature Family	61
95	B.0.1 SA Structure (Supplementary Alignment and Segment Met-	
96	rics)	61
97	B.0.2 Clipping-Based Features	63
98	B.0.3 K-mer Features	63
99	B.0.4 Microhomology Features	64
100	B.0.5 Others	64

¹⁰¹ List of Figures

¹⁰²	3.1 Process diagram of the study workflow.	20
¹⁰³	4.1 Boxplots of selected features for clean and chimeric reads.	39
¹⁰⁴	4.2 Feature correlation heatmap showing relationships among alignment-derived and sequence-derived features.	41
¹⁰⁵		
¹⁰⁶	4.3 Test F1 of all baseline classifiers.	43
¹⁰⁷	4.4 Comparison of test F1 (left) and ROC–AUC (right) for baseline	
¹⁰⁸	and tuned models.	44
¹⁰⁹		
¹¹⁰	4.5 Confusion matrices for the four representative models on the held-out test set.	47
¹¹¹		
¹¹²	4.6 ROC (left) and precision–recall (right) curves for the four representative models on the held-out test set.	48
¹¹³		
¹¹⁴	4.7 Permutation-based feature importance for four representative classifiers.	50

115	4.8 Aggregated feature family importance across four models.	52
116	4.9 Cumulative importance curve of features sorted by importance. .	53
117	4.10 Comparison of F1 and ROC–AUC for the full, top-4 selected, and	
118	no-microhomology feature set variants.	54
119	B.1 Boxplots of SA Structure features by class (1/2).	61
120	B.2 Boxplots of SA Structure features by class (2/2).	62
121	B.3 Boxplots of clipping-based features by class.	63
122	B.4 Boxplots of k-mer features by class.	63
123	B.5 Boxplots of microhomology features by class.	64
124	B.6 Boxplots of other numeric features by class.	64

125 List of Tables

¹³⁴ Chapter 1

¹³⁵ Introduction

¹³⁶ 1.1 Overview

¹³⁷ The rapid advancement of next-generation sequencing (NGS) technologies has
¹³⁸ transformed genomic research by enabling high-throughput and cost-effective
¹³⁹ DNA analysis (Metzker, 2010). Among current platforms, Illumina sequencing
¹⁴⁰ remains the most widely adopted, capable of producing millions of short reads
¹⁴¹ that can be assembled into reference genomes or analyzed for genetic variation
¹⁴² (Bentley et al., 2008; Glenn, 2011). Despite its high base-calling accuracy,
¹⁴³ Illumina sequencing is prone to artifacts introduced during library preparation,
¹⁴⁴ particularly polymerase chain reaction (PCR)-induced chimeras, which are ar-
¹⁴⁵ tificial hybrid sequences that do not exist in the true genome (Judo, Wedel, &
¹⁴⁶ Wilson, 1998).

¹⁴⁷ PCR chimeras form when incomplete extension products from one template

anneal to an unrelated DNA fragment and are extended, creating recombinant reads (Qiu et al., 2001). In mitochondrial genome assembly, such artifacts are especially problematic because the mitochondrial genome is small, circular, and often repetitive (Boore, 1999; Cameron, 2014). Even a small number of chimeric or misjoined reads can reduce assembly contiguity and introduce false junctions during organelle genome reconstruction (Dierckxsens, Mardulyn, & Smits, 2017; Hahn, Bachmann, & Chevreux, 2013; Jin et al., 2020). Existing assembly tools such as GetOrganelle and MITObim assume that input reads are largely free of such artifacts (Hahn et al., 2013; Jin et al., 2020). Consequently, undetected chimeras may produce fragmented assemblies or misidentified organellar boundaries. To ensure accurate reconstruction of mitochondrial genomes, a reliable method for detecting PCR-induced chimeras before assembly is essential.

This study focuses on mitochondrial sequencing data from the genus *Sardinella*, a group of small pelagic fishes widely distributed in Philippine waters. Among them, *Sardinella lemuru* (Bali sardinella) is one of the country's most abundant and economically important species, providing protein and livelihood to coastal communities (Labrador, Agmata, Palermo, Ravago-Gotanco, & Pante, 2021; Willette, Bognot, Mutia, & Santos, 2011). Accurate mitochondrial assemblies are critical for understanding its population genetics, stock structure, and evolutionary history. However, assembly pipelines often encounter errors or fail to complete due to undetected chimeric reads. To address this gap, this research introduces MitoChime, a machine learning pipeline designed to detect PCR-induced chimeric reads using both alignment-based and sequence-derived statistical features. The tool aims to provide bioinformatics laboratories, particularly the Philippine Genome Center Visayas (PGC Visayas), with an efficient

₁₇₃ solution for improving mitochondrial genome reconstruction.

₁₇₄ 1.2 Problem Statement

₁₇₅ Chimeric reads can distort assembly graphs and cause misassemblies, with par-
₁₇₆ ticularly severe effects in mitochondrial genomes (Boore, 1999; Cameron, 2014).
₁₇₇ Existing assembly pipelines such as GetOrganelle, MITObim, and NOVOPlasty
₁₇₈ assume that sequencing reads are free of such artifacts (Dierckxsens et al., 2017;
₁₇₉ Hahn et al., 2013; Jin et al., 2020). At PGC Visayas, several mitochondrial as-
₁₈₀ semblies have failed or yielded incomplete contigs despite sufficient coverage, sug-
₁₈₁ gesting that undetected chimeric reads compromise assembly reliability. Mean-
₁₈₂ while, existing chimera detection tools such as UCHIME and VSEARCH were
₁₈₃ developed primarily for amplicon-based community analysis and rely heavily on
₁₈₄ reference or taxonomic comparisons (Edgar, Haas, Clemente, Quince, & Knight,
₁₈₅ 2011; Rognes, Flouri, Nichols, Quince, & Mahé, 2016). These approaches are un-
₁₈₆ suitable for single-species organellar data, where complete reference genomes are
₁₈₇ often unavailable.

₁₈₈ 1.3 Research Objectives

₁₈₉ 1.3.1 General Objective

₁₉₀ This study aims to develop and evaluate a machine learning-based pipeline (Mi-
₁₉₁ toChime) that detects PCR-induced chimeric reads in *Sardinella lemuru* mito-

192 chondrial sequencing data in order to improve the quality and reliability of down-
193 stream mitochondrial genome assemblies.

194 **1.3.2 Specific Objectives**

195 Specifically, the study aims to:

- 196 1. construct simulated *Sardinella lemuru* Illumina paired-end datasets contain-
197 ing both clean and PCR-induced chimeric reads,
- 198 2. extract alignment-based and sequence-based features such as k-mer compo-
199 position, junction complexity, and split-alignment counts from both clean and
200 chimeric reads,
- 201 3. train, validate, and compare supervised machine learning models for classi-
202 fying reads as clean or chimeric,
- 203 4. determine feature importance and identify indicators of PCR-induced
204 chimerism,
- 205 5. integrate the optimized classifier into a modular and interpretable pipeline
206 deployable on standard computing environments at PGC Visayas.

207 **1.4 Scope and Limitations of the Research**

208 This study focuses solely on PCR-induced chimeric reads in *Sardinella lemuru*
209 mitochondrial sequencing data, with the species choice guided by four consid-
210 erations: (1) to limit interspecific variation in mitochondrial genome size, GC

211 content, and repetitive regions so that differences in read patterns can be at-
212 tributed more directly to PCR-induced chimerism, (2) to align the analysis with
213 relevant *S. lemuru* sequencing projects at PGC Visayas, (3) to take advantage of
214 the availability of *S. lemuru* mitochondrial assemblies and raw datasets in public
215 repositories such as the National Center for Biotechnology Information (NCBI),
216 which facilitates reference selection and benchmarking, and (4) to develop a tool
217 that directly supports local studies on *S. lemuru* population structure and fisheries
218 management.

219 The study emphasizes `wgsim`-based simulations and selected empirical mito-
220 chondrial datasets from *S. lemuru*. It excludes naturally occurring chimeras, nu-
221 clear mitochondrial pseudogenes (NUMTs), and large-scale assembly rearrange-
222 ments in nuclear genomes. Feature extraction is restricted to low-dimensional
223 alignment and sequence statistics, such as k-mer frequency profiles, GC con-
224 tent, soft and hard clipping metrics, and split-alignment counts rather than high-
225 dimensional deep learning embeddings. This design keeps model behaviour inter-
226 pretable and ensures that the pipeline can be run on standard workstations at
227 PGC Visayas. Testing on long-read platforms (e.g., Nanopore, PacBio) and other
228 taxa is outside the scope of this project.

229 Other limitations in this study include the following: simulations with vary-
230 ing error rates were not performed, so the effect of different sequencing errors on
231 model performance remains unexplored; alternative parameter settings, including
232 k-mer lengths and microhomology window sizes, were not systematically tested,
233 which could affect the sensitivity of both k-mer and microhomology feature de-
234 tection; and the machine learning models rely on supervised training with labeled
235 examples, which may limit their ability to detect novel or unexpected chimeric

²³⁶ patterns.

²³⁷ 1.5 Significance of the Research

²³⁸ This research provides both methodological and practical contributions to mito-
²³⁹ chondrial genomics and bioinformatics. First, MitoChime detects PCR-induced
²⁴⁰ chimeric reads prior to genome assembly, with the goal of improving the con-
²⁴¹ tiguity and correctness of *Sardinella lemuru* mitochondrial assemblies. Second,
²⁴² it replaces informal manual curation with a documented workflow, improving au-
²⁴³ tomation and reproducibility. Third, the pipeline is designed to run on computing
²⁴⁴ infrastructures commonly available in regional laboratories, enabling routine use
²⁴⁵ at facilities such as PGC Visayas. Finally, more reliable mitochondrial assemblies
²⁴⁶ for *S. lemuru* provide a stronger basis for downstream applications in the field of
²⁴⁷ fisheries and genomics.

²⁴⁸ **Chapter 2**

²⁴⁹ **Review of Related Literature**

²⁵⁰ This chapter presents an overview of the literature relevant to the study. It
²⁵¹ discusses the biological and computational foundations underlying mitochondrial
²⁵² genome analysis and assembly, as well as existing tools, algorithms, and techniques
²⁵³ related to chimera detection and genome quality assessment. The chapter aims to
²⁵⁴ highlight the strengths, limitations, and research gaps in current approaches that
²⁵⁵ motivate the development of the present study.

²⁵⁶ **2.1 The Mitochondrial Genome**

²⁵⁷ Mitochondrial genome (mtDNA) is a small, typically circular molecule found in
²⁵⁸ most eukaryotes. It encodes essential genes involved in oxidative phosphorylation
²⁵⁹ and energy metabolism. Because of its conserved structure, mtDNA has become
²⁶⁰ a valuable genetic marker for studies in population genetics and phylogenetics
²⁶¹ (Anderson et al., 1981; Boore, 1999). In animal species, the mitochondrial genome

ranges from 15–20 kilobase and contains 13 protein-coding genes, 22 tRNAs, and two rRNAs arranged compactly without introns (Gray, 2012). In comparison to nuclear DNA, the ratio of the number of copies of mtDNA is higher and has simple organization which make it particularly suitable for genome sequencing and assembly studies (Dierckxsens et al., 2017).

2.1.1 Mitochondrial Genome Assembly

Mitochondrial genome assembly refers to the reconstruction of the complete mitochondrial DNA (mtDNA) sequence from raw or fragmented sequencing reads. It is conducted to obtain high-quality, continuous representations of the mitochondrial genome that can be used for a wide range of analyses, including species identification, phylogenetic reconstruction, evolutionary studies, and investigations of mitochondrial diseases. Because mtDNA evolves rapidly, its assembled sequence provides valuable insights into population structure, lineage divergence, and adaptive evolution across taxa (Boore, 1999). Compared to nuclear genome assembly, assembling the mitochondrial genome is often considered more straightforward but still encounters technical challenges such as the formation of chimeric reads. Commonly used tools for mitogenome assembly such as GetOrganelle and MITObim operate under the assumption of organelle genome circularity, and are vulnerable when chimeric reads disrupt this circular structure, resulting in assembly errors (Hahn et al., 2013; Jin et al., 2020).

282 2.2 PCR Amplification and Chimera Formation

283 PCR plays an important role in NGS library preparation, as it amplifies target
284 DNA fragments for downstream analysis. However as previously mentioned, the
285 amplification process can also introduce chimeric reads which compromises the
286 quality of the input reads supplied to sequencing or assembly workflows. Chimeras
287 typically arise when incomplete extension occurs during a PCR cycle. This causes
288 the DNA polymerase to switch from one template to another and generate hy-
289 brid recombinant molecules (Judo et al., 1998). Artificial chimeras are produced
290 through such amplification errors, whereas biological chimeras occur naturally
291 through genomic rearrangements or transcriptional events.

292 In the context of amplicon-based sequencing, the presence of chimeras can in-
293 flate estimates of genetic or microbial diversity and may cause misassemblies dur-
294 ing genome reconstruction. Qin et al. (2023) has reported that chimeric sequences
295 may account for more than 10% of raw reads in amplicon datasets. This artifact
296 tends to be most prominent among rare operational taxonomic units (OTUs) or
297 singletons, which are sometimes misinterpreted as novel diversity, further caus-
298 ing the complication of microbial diversity analyses (Gonzalez, Zimmermann, &
299 Saiz-Jimenez, 2004). As such, determining and minimizing PCR-induced chimera
300 formation is vital for improving the quality of mitochondrial genome assemblies,
301 and ensuring the reliability of amplicon sequencing data.

302 **2.3 Existing Traditional Approaches for Chimera**

303 **Detection**

304 Several computational tools have been developed to identify chimeric sequences in
305 NGS datasets. These tools generally fall into two categories: reference-based and
306 de novo approaches. Reference-based chimera detection, also known as database-
307 dependent detection, is one of the earliest and most widely used computational
308 strategies for identifying chimeric sequences in amplicon-based community studies.
309 These methods rely on the comparison of each query sequence against a curated,
310 high-quality database of known, non-chimeric reference sequences (Edgar et al.,
311 2011).

312 On the other hand, the de novo chimera detection, also referred to as reference-
313 free detection, represents an alternative computational paradigm that identifies
314 chimeric sequences without reliance on external reference databases. This method
315 infer chimeras based on internal relationships among the sequences present within
316 the dataset itself, making it particularly advantageous in studies of under explored
317 or taxonomically diverse communities where comprehensive reference databases
318 are unavailable or incomplete (Edgar, 2016; Edgar et al., 2011). The underlying
319 assumption on this method is that during PCR, true biological sequences are
320 generally more abundant as they are amplified early and dominate the read pool,
321 whereas chimeric sequences appear later and are generally less abundant. The
322 de novo approach leverage this abundance hierarchy, treating the most abundant
323 sequences as supposed parents and testing whether less abundant sequences can
324 be reconstructed as mosaics of these templates. Compositional and structural
325 similarity are also evaluated to check whether different regions of a candidate

326 sequence correspond to distinct high-abundance sequences.

327 In practice, many modern bioinformatics pipelines combine both paradigms
328 sequentially: an initial de novo step identifies dataset-specific chimeras, followed
329 by a reference-based pass that removes remaining artifacts relative to established
330 databases (Edgar, 2016). These two methods of detection form the foundation of
331 tools such as UCHIME and later UCHIME2.

332 2.3.1 UCHIME

333 UCHIME is one of the most widely used tools for detecting chimeric sequences in
334 amplicon-based studies and remains a standard quality-control step in microbial
335 community analysis. Its core strategy is to test whether a query sequence (Q) can
336 be explained as a mosaic of two parent sequences, (A and B), and to score this
337 relationship using a structured alignment model (Edgar et al., 2011).

338 In reference mode, UCHIME divides the query into several segments and maps
339 them against a curated database of non-chimeric sequences. Candidate parents
340 are identified, and a three-way alignment is constructed. The algorithm assigns
341 “Yes” votes when different segments of the query match different parents and
342 “No” votes when the alignment contradicts a chimeric pattern. The final score
343 reflects the balance of these votes. In de novo mode, UCHIME operationalizes the
344 abundance-skew principle described earlier: high-abundance sequences are treated
345 as candidate parents, and lower-abundance sequences are evaluated as potential
346 mosaics. This makes the method especially useful when no reliable reference
347 database exists.

348 Although UCHIME is highly sensitive, it faces key constraints. Chimeras
349 formed from parents with very low divergence (below 0.8%) are difficult to detect
350 because they are nearly indistinguishable from sequencing errors. Accuracy in ref-
351 erence mode depends strongly on database completeness, while de novo detection
352 assumes that true parents are both present and sufficiently more abundant, such
353 conditions are not always met.

354 **2.3.2 UCHIME2**

355 UCHIME2 extends the original algorithm with refinements tailored for high-
356 resolution sequencing data. One of its major contributions is a re-evaluation
357 of benchmarking practices. Edgar (2016) demonstrated that earlier accuracy es-
358 timates for chimera detection were overly optimistic because they relied on un-
359 realistic scenarios where all true parent sequences were assumed to be present.
360 Using the more rigorous CHSIMA benchmark, UCHIME2 showed the prevalence
361 of “fake models” or real biological sequences that can be perfectly reconstructed
362 as apparent chimeras of other sequences, which suggests that perfect chimera de-
363 tection is theoretically unattainable. UCHIME2 also introduces several preset
364 modes (e.g., denoised, balanced, sensitive, specific, high-confidence) designed to
365 tune sensitivity and specificity depending on dataset characteristics. These modes
366 allow users to adjust the algorithm to the expected noise level or analytical goals.

367 Despite these improvements, UCHIME2 must be applied with caution. The
368 website manual explicitly advises against using UCHIME2 as a standalone
369 chimera-filtering step in OTU clustering or denoising workflows because doing so
370 can inflate both false positives and false negatives (Edgar, n.d.).

371 2.3.3 CATch

372 As previously mentioned, UCHIME (Edgar et al., 2011) relied on alignment-based
373 sequences in amplicon data. However, researchers soon observed that different al-
374 gorithms often produced inconsistent predictions. A sequence might be identified
375 as chimeric by one tool but classified as non-chimeric by another, resulting in
376 unreliable filtering outcomes across studies.

377 To address these inconsistencies, Mysara, Saeys, Leys, Raes, and Monsieurs
378 (2015) developed the Classifier for Amplicon Tool Chimeras (CATCh), which rep-
379 resents the first ensemble machine learning system designed for chimera detection
380 in 16S rRNA amplicon sequencing. Rather than depending on a single detec-
381 tion strategy, CATCh integrates the outputs of several established tools, includ-
382 ing UCHIME, ChimeraSlayer, DECIPHER, Pintail, and Perseus. The individual
383 scores and binary decisions generated by these tools are used as input features for
384 a supervised learning model. The algorithm employs a Support Vector Machine
385 (SVM) with a Pearson VII Universal Kernel (PUK) to determine optimal weight-
386 ings among the input features and to assign each sequence a probability of being
387 chimeric.

388 Benchmarking in both reference-based and de novo modes demonstrated signif-
389 icant performance improvements. CATCh achieved sensitivities of approximately
390 85 percent in reference-based mode and 92 percent in de novo mode, with corre-
391 sponding specificities of approximately 96 percent and 95 percent. These results
392 indicate that CATCh detected 7 to 12 percent more chimeras than any individual
393 algorithm while maintaining high precision.

394 **2.3.4 ChimPipe**

395 Among the available tools for chimera detection, ChimPipe is a pipeline developed
396 to identify chimeric sequences such as biological chimeras. It uses both discordant
397 paired-end reads and split-read alignments to improve the accuracy and sensitivity
398 of detecting biological chimeras (Rodriguez-Martin et al., 2017). By combining
399 these two sources of information, ChimPipe achieves better precision than meth-
400 ods that depend on a single type of indicator.

401 The pipeline works with many eukaryotic species that have available genome
402 and annotation data (Rodriguez-Martin et al., 2017). It can also predict multiple
403 isoforms for each gene pair and identify breakpoint coordinates that are useful
404 for reconstructing and verifying chimeric transcripts. Tests using both simulated
405 and real datasets have shown that ChimPipe maintains high accuracy and reliable
406 performance.

407 ChimPipe lets users adjust parameters to fit different sequencing protocols or
408 organism characteristics. Experimental results have confirmed that many chimeric
409 transcripts detected by the tool correspond to functional fusion proteins, demon-
410 strating its utility for understanding chimera biology and its potential applications
411 in disease research (Rodriguez-Martin et al., 2017).

412 **2.4 Machine Learning Approaches for Chimera**

413 **and Sequence Quality Detection**

414 Traditional chimera detection tools rely primarily on heuristic or alignment-based
415 rules. Recent advances in machine learning (ML) have demonstrated that models
416 trained on sequence-derived features can effectively capture compositional and
417 structural patterns in biological sequences. Although most existing ML systems
418 such as those used for antibiotic resistance prediction, taxonomic classification,
419 or viral identification are not specifically designed for chimera detection, they
420 highlight how data-driven models can outperform similarity-based heuristics by
421 learning intrinsic sequence signatures. In principle, ML frameworks can integrate
422 indicators such as k-mer frequencies, GC-content variation and split-alignment
423 metrics to identify subtle anomalies that may indicate a chimeric origin (Arango
424 et al., 2018; Liang, Bible, Liu, Zou, & Wei, 2020; Ren et al., 2020).

425 **2.4.1 Feature-Based Representations of Genomic Se-**

426 **quences**

427 Feature extraction converts DNA sequences into numerical representations suit-
428 able for machine learning models. One approach is k-mer frequency analysis,
429 which counts short nucleotide sequences within a read (Vervier, Mahé, Tournoud,
430 Veyrieras, & Vert, 2015). High-frequency k-mers, including simple repeats such
431 as “AAAAAA,” can highlight repetitive or unusual regions that may occur near
432 chimeric junctions. Comparing k-mer patterns across adjacent parts of a read can
433 help identify such regions, while GC content provides an additional descriptor of

434 local sequence composition (Ren et al., 2020).

435 Alignment-derived features further inform junction detection. Long-read tools
436 such as Sniffles (Sedlazeck et al., 2018) use split alignments to locate breakpoints
437 across extended sequences, whereas short-read aligners like Minimap2 (Li, 2018)
438 report supplementary and secondary alignments that indicate local discontinu-
439 ities. Split alignments, where parts of a read map to different regions, can reveal
440 template-switching events. These features complement k-mer profiles and en-
441 hance detection of potentially chimeric reads, even in datasets with incomplete
442 references.

443 Microhomology, or short sequences shared between adjacent segments, is an-
444 other biologically meaningful feature. Short microhomologies, typically 3–20 bp,
445 are involved in template switching both in cellular repair pathways and during
446 PCR, where they act as signatures of chimera formation (Peccoud et al., 2018;
447 Sfeir & Symington, 2015). In PCR-induced chimeras, short identical sequences
448 at junctions provide a clear signature of chimerism. Measuring the longest exact
449 overlap at each breakpoint complements k-mer and alignment features and helps
450 identify reads that are potentially chimeric.

451 **2.5 Synthesis of Chimera Detection Approaches**

452 To provide an integrated overview of the literature discussed in this chapter, Ta-
453 ble 2.1 summarizes the major chimera detection studies, their methodological
454 approaches, and their known limitations.

Table 2.1: Comparison of Chimera Detection Approaches and Tools

Method / Tool	Core Approach	Key Limitations
Reference-based Detection	Compares each query sequence against curated databases of verified, non-chimeric sequences; evaluates segment similarity to identify mosaic patterns.	Accuracy depends on database completeness; performs poorly for novel taxa or missing parents; limited sensitivity for low-divergence chimeras.
De novo Detection	Identifies chimeras using only internal dataset structure; leverages abundance hierarchy and compositional similarity to infer whether low-abundance sequences can be reconstructed from abundant parents.	Assumes true sequences are more abundant; fails when amplification bias distorts abundances; struggles when parental sequences are similarly abundant or highly similar.
UCHIME	Alignment-based model that partitions the query into segments, identifies parent candidates, and computes a chimera score via a three-way alignment; supports reference and de novo modes.	Reduced accuracy for very closely related parents (<0.8% divergence); sensitive to incomplete databases; de novo mode fails if parents are absent or not sufficiently more abundant.
UCHIME2	Updated UCHIME with improved benchmarking (CHSIMA) and multiple sensitivity/specificity presets; better handles incomplete references and dataset variability.	“Fake models” limit theoretical accuracy; genuine variants may mimic chimeras; not recommended as a standalone step in OTU or denoising pipelines due to increased false positives/negatives.
CATCh	First ensemble ML model for 16S chimera detection; integrates outputs of UCHIME, ChimeraSlayer, DECIPHER, Pintail, and Perseus using an SVM to boost overall prediction accuracy.	Performance constrained by underlying tools; ML model cannot capture features not present in component algorithms; may misclassify in highly novel or low-coverage datasets.
ChimPipe	Pipeline for detecting biological chimeras in RNA-seq using discordant paired-end reads and split-read alignments; identifies isoforms and breakpoint coordinates.	Requires high-quality genome and annotation; tailored to RNA-seq rather than amplicons; computationally intensive; limited to organisms with available reference genomes.

455 Across existing studies, no single approach reliably detects all forms of chimeric
456 sequences, and the reviewed literature consistently shows that chimeras remain a
457 persistent challenge in genomics and bioinformatics. Although the surveyed tools
458 are not designed specifically for organelle genome assembly, they provide valua-
459 ble insights into which methodological strategies are effective and where current
460 approaches fall short. These limitations collectively define a clear research gap:
461 the need for a specialized, feature-driven detection framework tailored to PCR-
462 induced mitochondrial chimeras. Addressing this gap aligns with the research
463 objective outlined in Section 1.3, which is to develop and evaluate a machine
464 learning-based pipeline (MitoChime) that improves the quality of downstream
465 mitochondrial genome assembly. In support of this aim, the subsequent chapters
466 describe the design, implementation, and evaluation of the proposed tool.

⁴⁶⁷ Chapter 3

⁴⁶⁸ Research Methodology

⁴⁶⁹ This chapter outlines the steps involved in completing the study, including data
⁴⁷⁰ gathering, generating simulated mitochondrial Illumina reads, preprocessing and
⁴⁷¹ indexing the data, developing a feature extraction pipeline to obtain read-level fea-
⁴⁷² tures, applying machine learning algorithms for chimera detection, implementing
⁴⁷³ feature selection methods, and validating and comparing model performance.

⁴⁷⁴ 3.1 Research Activities

⁴⁷⁵ As illustrated in Figure 3.1, this study carried out a sequence of procedures to
⁴⁷⁶ detect PCR-induced chimeric reads in mitochondrial genomes. The process began
⁴⁷⁷ with collecting a mitochondrial reference sequence of *Sardinella lemuru* from the
⁴⁷⁸ National Center for Biotechnology Information (NCBI) database, which was used
⁴⁷⁹ as a reference for generating simulated clean and chimeric reads. These reads
⁴⁸⁰ were subsequently indexed and mapped. The resulting collections then passed

481 through a feature extraction pipeline that computed k-mer profiles, supplementary
482 alignment (SA) features, and microhomology information to prepare the data
483 for model construction. The machine learning models were trained using the
484 processed input, evaluated using cross-validation and held-out testing, tuned for
485 improved performance, and then subjected to feature importance and feature
486 selection analyses before final validation.

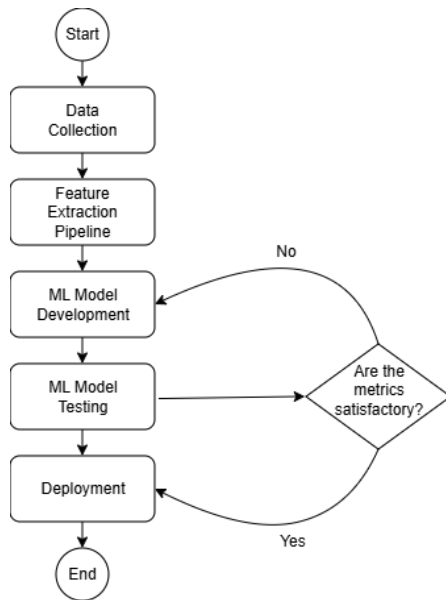


Figure 3.1: Process diagram of the study workflow.

487 3.1.1 Data Collection

488 The mitochondrial genome reference sequence of *S. lemuru* was obtained from the
489 NCBI database (accession number NC_039553.1) in FASTA format and was used
490 to generate simulated reads.

491 This step was scheduled to begin in the first week of November 2025 and
492 expected to be completed by the end of that week, with a total duration of ap-

493 proximately one (1) week.

494 **Data Preprocessing**

495 All steps in the simulation and preprocessing pipeline were executed using a cus-
496 tom script in Python (Version 3.11). The script runs each stage, including read
497 simulation, reference indexing, mapping, and alignment processing, in a fixed se-
498 quence.

499 `wgsim` (Version 1.13) was used to simulate 10,000 paired-end fragments, pro-
500 ducing 20,000 reads (10,000 forward and 10,000 reverse) from the original refer-
501 ence (`original_reference.fasta`) and designated as clean reads. The tool was
502 selected because it provides fast generation of Illumina-like reads with controllable
503 error rates, using the following command:

```
504 wgsim -1 150 -2 150 -r 0 -R 0 -X 0 -e 0.05 -N 10000 \  
505           original_reference.fasta ref1.fastq ref2.fastq
```

506 Chimeric sequences were then generated from the same reference FASTA
507 file using a separate Python script. Two non-adjacent segments were ran-
508 domly selected such that their midpoint distances fell within specified minimum
509 and maximum thresholds. The script attempted to retain microhomology to
510 mimic PCR-induced template switching. The resulting chimeras were written
511 to `chimera_reference.fasta` and processed with `wgsim` to simulate 10,000
512 paired-end fragments, generating 20,000 chimeric reads (10,000 forward reads in
513 `chimeric1.fastq` and 10,000 reverse reads in `chimeric2.fastq`) using the same
514 command format as above.

515 Next, a `minimap2` index of the reference genome was created using:

```
516  minimap2 -d ref.mmi original_reference.fasta
```

517 Minimap2 (Version 2.28) was used to map simulated clean and chimeric reads
518 to the original reference. An index (`ref.mmi`) was first generated to enable efficient
519 alignment, and mapping produced the alignment features used as input for the
520 machine learning model. The reads were mapped using the following commands:

```
521  minimap2 -ax sr -t 8 ref.mmi ref1.fastq ref2.fastq > clean.sam
```

```
522  minimap2 -ax sr -t 8 ref.mmi \  
523      chimeric1.fastq chimeric2.fastq > chimeric.sam
```

524 The resulting clean and chimeric SAM files contain the alignment positions of
525 each read relative to the original reference genome. These files were then converted
526 to BAM format, sorted, and indexed using `samtools` (Version 1.20):

```
527  samtools view -bS clean.sam -o clean.bam  
528  samtools view -bS chimeric.sam -o chimeric.bam  
529  
530  samtools sort clean.bam -o clean.sorted.bam  
531  samtools index clean.sorted.bam  
532  
533  samtools sort chimeric.bam -o chimeric.sorted.bam  
534  samtools index chimeric.sorted.bam
```

535 The total number of simulated reads was expected to be 40,000. The final col-
536 lection of reads contained 19,984 clean reads and 20,000 chimeric reads (39,984 en-
537 tries in total), providing a roughly balanced distribution between the two classes.
538 After alignment with `minimap2`, only 19,984 clean reads remained because un-
539 mapped reads were not included in the BAM file. Some sequences failed to align
540 due to the error rate defined during `wgsim` simulation, which produced mismatches
541 that caused certain reads to fall below the aligner’s matching threshold.

542 This whole process was scheduled to start in the second week of November 2025
543 and was expected to be completed by the last week of November 2025, with a total
544 duration of approximately three (3) weeks.

545 **3.1.2 Feature Extraction Pipeline**

546 This stage directly followed the alignment phase, utilizing the resulting BAM files
547 (specifically `chimeric.sorted.bam` and `clean.sorted.bam`). A custom Python
548 script was created to efficiently process each primary-mapped read to extract
549 the necessary set of features, which were then compiled into a structured feature
550 matrix in TSV format. The pipeline’s core functionality relied on the `Pysam`
551 (Version 0.22) library for parsing BAM structures and `NumPy` (Version 1.26) for
552 array operations and computations. To ensure correctness and adherence to best
553 practices, bioinformatics experts at PGC Visayas were consulted to validate the
554 pipeline design, feature extraction logic, and overall data integrity.

555 This stage of the study was scheduled to begin in the last week of Novem-
556 ber 2025 and conclude by the first week of December 2025, with an estimated

557 total duration of approximately two (2) weeks.

558 The pipeline focused on three feature families that collectively capture bi-
559 ological signatures associated with PCR-induced chimeras: (1) supplementary
560 alignment (SA) and alignment-structure metrics, (2) k-mer composition differ-
561 ence, and (3) microhomology around putative junctions. Additional alignment
562 quality indicators such as mapping quality were also included.

563 **Supplementary Alignment and Alignment-Structure Features**

564 Split-alignment information was derived from the SA tag embedded in each pri-
565 mary read of the BAM file. This tag is typically associated with reads that map to
566 multiple genomic locations, suggesting a chimeric structure. To extract this infor-
567 mation, the script first checked whether the read carried an **SA:Z** tag. If present,
568 the tag string was parsed using the function **parse_sa_tag**, yielding metadata for
569 each alignment containing the reference name, mapped position, strand, mapping
570 quality, and number of mismatches.

571 After parsing, the function **sa_feature_stats** was applied to establish the fun-
572 damental split indicators, **has_sa** and **sa_count**. Along with these initial counts,
573 the function aggregated metrics related to the structure and reliability of the
574 split alignments, including the number of alignment segments, strand consistency,
575 minimum, maximum, and mean distance between split segments, and summary
576 statistics of mapping quality and mismatch counts across segments.

577 **K-mer Composition Difference**

578 Comparing k-mer frequency profiles between the left and right halves of a read
579 allows for the detection of abrupt compositional shifts, independent of alignment
580 information.

581 The script implemented this by inferring a likely junction breakpoint using the
582 function `infer_breakpoints`, prioritizing the boundaries defined by soft-clipping
583 operations. If no clipping was present, the midpoint of the alignment or the read
584 length was used as a fallback. The read sequence was then divided into left and
585 right segments at this inferred breakpoint, and k-mer frequency profiles ($k =$
586 6) were generated for both halves, ignoring any k-mers containing ambiguous N
587 bases. The resulting k-mer frequency vectors were normalised and compared using
588 the functions `cosine_difference` and `js_divergence` to quantify compositional
589 discontinuity across the inferred breakpoint.

590 **Microhomology**

591 The process of extracting the microhomology feature also started by using
592 `infer_breakpoints` to identify a candidate junction. Once a breakpoint was
593 established, the script scanned a ± 40 base-pair window surrounding the break-
594 point and applied the function `longest_suffix_prefix_overlap` to identify the
595 longest exact suffix-prefix overlap between the left and right read segments. This
596 overlap, representing consecutive bases shared at the junction, was recorded as
597 `microhomology_length` in the dataset. The 40 base-pair window was chosen
598 to ensure that short shared sequences at or near the breakpoint were captured

599 without including distant sequences that are unlikely to be mechanistically
600 related.

601 Additionally, the GC content of the overlapping sequence was calculated using
602 the function `gc_content`, which counts guanine (G) and cytosine (C) bases within
603 the detected microhomology and divides by the total length, yielding a proportion
604 between 0 and 1 that was stored under the `microhomology_gc` attribute. Micro-
605 homology was quantified using a 3–20 bp window, consistent with values reported
606 in prior research on PCR-induced chimeras. A k-mer length of 6 was used to cap-
607 ture patterns within the 40 bp window surrounding each breakpoint, providing
608 sufficient resolution to detect informative sequence shifts.

609 3.1.3 Machine Learning Model Development

610 After feature extraction, the per-read feature matrices for clean and chimeric
611 reads were merged into a single dataset. Each row corresponded to one paired-
612 end read, and columns encoded alignment-structure features (e.g., supplementary
613 alignment count and spacing between segments), CIGAR-derived soft-clipping
614 statistics (e.g., left and right soft-clipped length, total clipped bases), k-mer com-
615 position discontinuity between read segments, microhomology descriptors near
616 candidate junctions, and alignment quality (e.g., mapping quality). The result-
617 ing feature set comprised 23 numeric features and was restricted to quantities
618 that can be computed from standard BAM/FASTQ files in typical mitochondrial
619 sequencing workflows.

620 The labelled dataset was randomly partitioned into training (80%) and test

621 (20%) subsets using stratified sampling to preserve the 1:1 ratio of clean to
622 chimeric reads. Model development and evaluation were implemented in Python
623 (Version 3.11) using the `scikit-learn`, `xgboost`, `lightgbm`, and `catboost` li-
624 braries. A broad panel of classification algorithms was then benchmarked on the
625 training data to obtain a fair comparison of different model families under identical
626 feature conditions. The panel included a trivial dummy classifier, L_2 -regularized
627 logistic regression, a calibrated linear support vector machine (SVM), k -nearest
628 neighbours, Gaussian Naïve Bayes, decision-tree ensembles (Random Forest, Ex-
629 tremely Randomized Trees, and Bagging with decision trees), gradient boosting
630 methods (Gradient Boosting, XGBoost, LightGBM, and CatBoost), and a shallow
631 multilayer perceptron (MLP).

632 For each model, five-fold stratified cross-validation was performed on the train-
633 ing set. In every fold, four-fifths of the data were used for fitting and the remaining
634 one-fifth for validation. Mean cross-validation accuracy, precision, recall, F1-score
635 for the chimeric class, and area under the receiver operating characteristic curve
636 (ROC–AUC) were computed to summarize performance and rank candidate meth-
637 ods. This baseline screen allowed comparison of linear, probabilistic, neural, and
638 ensemble-based approaches and identified tree-based ensemble and boosting mod-
639 els as consistently strong performers relative to simpler baselines.

640 **3.1.4 Model Benchmarking, Hyperparameter Optimiza- 641 tion, and Evaluation**

642 Model selection and refinement proceeded in two stages. First, the cross-validation
643 results from the broad panel were used to identify a subset of competitive mod-

els for more detailed optimization. Specifically, ten model families were carried forward: L_2 -regularized logistic regression, calibrated linear SVM, Random Forest, ExtraTrees, Gradient Boosting, XGBoost, LightGBM, CatBoost, Bagging with decision trees, and a shallow MLP. This subset spans both linear and non-linear decision boundaries, but emphasizes ensemble and boosting methods, which showed superior F1 and ROC–AUC in the initial benchmark.

Second, hyperparameter optimization was conducted for each of the ten selected models using randomized search with five-fold stratified cross-validation (`RandomizedSearchCV`). For tree-based ensembles, the search space included the number of trees, maximum depth, minimum samples per split and per leaf, and the fraction of features considered at each split. For boosting methods, key hyperparameters such as the number of boosting iterations, learning rate, tree depth, subsampling rate, and column subsampling rate were tuned. For the MLP, the number and size of hidden layers, learning rate, and L_2 -regularization strength were varied. In all cases, the primary optimisation criterion was the F1-score of the chimeric class, averaged across folds.

For each model family, the hyperparameter configuration with the highest mean cross-validation F1-score was selected as the best-tuned estimator. These tuned models were then refitted on the full training set and evaluated once on the held-out test set to obtain unbiased estimates of performance. Test-set metrics included accuracy, precision, recall, F1-score for the chimeric class, and ROC–AUC. Confusion matrices and ROC curves were generated for the top-performing models to characterise common error modes, such as false negatives (missed chimeric reads) and false positives (clean reads incorrectly labelled as chimeric). The final model or small set of models for downstream interpretation was chosen based on

669 a combination of test-set F1-score and ROC–AUC.

670 **3.1.5 Feature Importance, Feature Selection, and Inter-**
671 **pretation**

672 To relate model decisions to biologically meaningful signals, feature-importance
673 analyses were performed on the best-performing tree-based models. Two comple-
674 mentary approaches were used. First, built-in importance measures from ensemble
675 methods (e.g., split-based importances in Random Forest and Gradient Boosting)
676 were examined to obtain an initial ranking of features based on their contributon
677 to reducing impurity. Second, model-agnostic permutation importance was com-
678 puted on the test set by repeatedly permuting each feature column while keeping
679 all others fixed and measuring the resulting decrease in F1-score. Features whose
680 permutation led to a larger performance drop were interpreted as more influential
681 for chimera detection.

682 For interpretability, individual features were grouped into conceptual families:
683 (i) supplementary alignment and alignment-structure features (e.g., SA count,
684 spacing between alignment segments, strand consistency), (ii) soft-clipping fea-
685 tures (e.g., left and right soft-clipped length, total clipped bases, inferred break-
686 point position), (iii) k-mer composition discontinuity features (e.g., cosine dis-
687 tance and Jensen–Shannon divergence between k-mer profiles of read segments),
688 (iv) microhomology descriptors (e.g., microhomology length and local GC content
689 around putative breakpoints), and (v) other alignment quality features (e.g., map-
690 ping quality). This analysis provided a basis for interpreting the trained models
691 in terms of known mechanisms of PCR-induced template switching and for iden-

692 tifying which alignment-based and sequence-derived cues are most informative for
693 distinguishing chimeric from clean mitochondrial reads.

694 Building on these importance results, an explicit feature selection step was
695 implemented using CatBoost as the reference model, since it was among the top-
696 performing classifiers. Permutation importance scores were re-estimated for Cat-
697 Boost on the held-out test set using the F1-score of the chimeric class as the
698 scoring function. Negative importance scores, which indicate that permuting a
699 feature did not reliably harm performance, were set to zero and interpreted as
700 noise. The remaining non-negative importances were sorted in descending order
701 and converted into a cumulative importance curve by expressing each feature's
702 importance as a fraction of the total positive importance.

703 A compact feature subset was then defined by selecting the smallest number of
704 features whose cumulative importance reached at least 95% of the total positive
705 importance. This procedure yielded a reduced set of four strongly predictive
706 variables dominated by soft-clipping and k-mer divergence metrics (for example,
707 total clipped bases and k-mer divergence between read halves).

708 To quantify the impact of this reduction, CatBoost was retrained using only
709 the selected feature subset, with the same tuned hyperparameters as the full 23-
710 feature model, and evaluated on the held-out test set. Performance of the reduced
711 model was then compared to that of the full model in terms of F1-score and ROC–
712 AUC to assess whether dimensionality could be reduced without appreciable loss
713 in predictive accuracy.

714 In addition, an ablation experiment was performed to specifically evaluate
715 the contribution of explicit microhomology features. The microhomology vari-

ables (`microhomology_length` and `microhomology_gc`) were removed from the full feature set to obtain a 21-feature configuration. CatBoost was refitted on this microhomology-ablated feature set, using the same tuned hyperparameters, and evaluated on the held-out test set. Comparing the full, reduced-subset, and microhomology-ablated variants allowed the study to quantify both the degree of redundancy among features and the practical contribution of microhomology to classification accuracy.

Taken together, the feature importance and feature selection analyses provided a more parsimonious model variant and a clearer interpretation of which alignment-based and sequence-derived signals are most informative for detecting PCR-induced chimeras.

3.1.6 Validation and Testing

Validation involved both internal and external evaluations. Internal validation was achieved through five-fold stratified cross-validation on the training data to verify model generalization and reduce variance due to random sampling. External testing was performed on the 20% hold-out dataset from the simulated reads, providing an unbiased assessment of model generalization. Feature extraction and preprocessing were applied consistently across all splits.

Comparative evaluation was performed across all candidate algorithms and CatBoost feature-set variants to determine which models demonstrated the highest predictive performance and computational efficiency under identical data conditions. Their metrics were compared to identify which algorithms and feature

738 configurations were most suitable for further refinement and potential integration
739 into downstream mitochondrial assembly workflows.

740 3.1.7 Documentation

741 Comprehensive documentation was maintained throughout the study to ensure
742 transparency and reproducibility. All stages of the research, including data gath-
743 ering, preprocessing, feature extraction, model training, feature selection, and
744 validation, were systematically recorded in a `README` file in the GitHub reposi-
745 tory. For each analytical step, the corresponding parameters, software versions,
746 and command line scripts were documented to enable exact replication of results.

747 The repository structure followed standard research data management prac-
748 tices, with clear directories for datasets and scripts. Computational environments
749 were standardised using Conda, with an environment file (`environment.yml`)
750 specifying dependencies and package versions to maintain consistency across sys-
751 tems.

752 For manuscript preparation and supplementary materials, Overleaf (LATEX)
753 was used to produce publication-quality formatting and consistent referencing.

754 3.2 Calendar of Activities

755 Table 3.1 presents the project timeline in the form of a Gantt chart, where each
756 bullet point corresponds to approximately one week of planned activity.

Table 3.1: Timetable of activities.

Activities (2025)	Nov	Dec	Jan	Feb	Mar	Apr	May
Data Collection and Simulation	• • • •						
Feature Extraction Pipeline	•	•					
Machine Learning Development		•	• •	• • • •	• • • •	• •	
Testing and Validation						• •	• • • •
Documentation	• • • •	• • • •	• • • •	• • • •	• • • •	• • • •	• • • •

⁷⁵⁷ Chapter 4

⁷⁵⁸ Results and Discussion

⁷⁵⁹ This chapter presents the performance of the proposed feature set and machine
⁷⁶⁰ learning models for detecting PCR-induced chimeric reads in simulated mito-
⁷⁶¹ chondrial Illumina data. The behaviour of the extracted features is first examined
⁷⁶² through descriptive and correlation analyses, followed by a comparison of baseline
⁷⁶³ and tuned classifiers. The chapter then examines model performance in detail and
⁷⁶⁴ investigates the contribution of individual features and feature families, including
⁷⁶⁵ the impact of feature selection on classification performance.

⁷⁶⁶ The final dataset contained 31,986 reads for training and 7,997 reads for test-
⁷⁶⁷ ing, with classes balanced (approximately 4,000 clean and 4,000 chimeric reads in
⁷⁶⁸ the test split).

769 **4.1 Descriptive Analysis of Features**

770 **4.1.1 Summary Statistics Per Class**

771 Summary statistics were computed separately for clean reads (class 0) and
772 chimeric reads (class 1) to characterize the distributional behavior of the features.
773 For each feature, the mean, standard deviation, median, first and third quartiles
774 (Q1, Q3), interquartile range (IQR), minimum, maximum, and sample size (n)
775 were calculated.

776 Only a subset of the features is summarized in the main text to highlight key
777 trends, and not all summary statistics columns are shown for brevity. The com-
778 plete set of per-class summary statistics for all features is provided in Appendix A
779 (Table A.1).

780 **Alignment and Supplementary Alignment Features**

781 Features related to supplementary alignments show strong separation between
782 classes. Chimeric reads frequently exhibit supplementary alignments, reflected
783 by higher values of `has_sa`, `sa_count`, and `num_segments`, whereas clean reads
784 consistently show a single alignment segment with no supplementary mappings.
785 Table 4.1 shows that `has_sa` is present in chimeric reads (mean = 0.406) but absent
786 in clean reads (mean = 0.000), while `num_segments` increases from a constant value
787 of 1.000 in clean reads to a mean of 1.406 in chimeric reads. These patterns align
788 with the expected structure of chimeric reads and indicate that alignment-based
789 features are highly informative.

790 **Clipping-Based Features**

791 Clipping-related features, including `softclip_left`, `softclip_right`, and
792 `total_clipped_bases`, display higher values and broader distributions in chimeric
793 reads. In chimeric reads, `total_clipped_bases` reaches 25.44 on average, with a
794 median of 19.0 and an IQR of 48.0, while `softclip_left` and `softclip_right`
795 have averages of 12.55 and 12.90, medians of 0.0, and IQRs of 19.0. Clean
796 reads maintain values near zero across all these metrics. These patterns indi-
797 cate substantial clipping and increased variability in chimeric reads, reflecting
798 junction-like alignment fragmentation, whereas clean reads remain unaltered.

799 **K-mer Distribution Features**

800 K-mer-based features, including `kmer_js_divergence` and `kmer_cosine_diff`,
801 show only minor differences between clean and chimeric reads. In chimeric
802 reads, `kmer_js_divergence` has a mean of 0.974 with a median of 0.986, and
803 `kmer_cosine_diff` has a mean of 0.974 with a median of 0.986. Clean reads show
804 similar values, with `kmer_js_divergence` at 0.976 with a median of 0.986, and
805 `kmer_cosine_diff` at 0.976 with a median of 0.986. The close similarity of the
806 means, medians, and overall ranges of values indicates that these features alone
807 provide limited ability to distinguish clean from chimeric reads.

808 **Microhomology Features**

809 Microhomology-related features, including `microhomology_length` and
810 `microhomology_gc`, exhibit nearly identical summary statistics between clean

811 and chimeric reads. Most reads in both classes have short or zero-length micro-
812 homologies. Table 4.1 shows that `microhomology_gc` has a mean of 0.172 and
813 a median of 0.0 in both clean and chimeric reads, while `microhomology_length`
814 averages 0.458 with a median of 0.0 in chimeric reads and 0.462 with a median
815 of 0.0 in clean reads. These values indicate that microhomology features alone
816 provide limited discriminatory power and are more appropriately considered as
817 supporting evidence.

818 Overall, the summary statistics indicate that alignment-based and clipping-
819 based features provide the strongest class separation, k-mer features contribute
820 limited but complementary signal, and microhomology features exhibit minimal
821 discriminative power on their own. These observations motivate the combined
822 multi-feature approach used in subsequent modeling and evaluation.

Table 4.1: Summary statistics of selected key features by class.

Feature	Class	Mean	Std	Median	IQR
has_sa	chimeric	0.406	0.491	0.0	1.0
has_sa	clean	0.000	0.000	0.0	0.0
num_segments	chimeric	1.406	0.491	1.0	1.0
num_segments	clean	1.000	0.000	1.0	0.0
softclip_left	chimeric	12.55	21.90	0.0	19.0
softclip_left	clean	0.23	1.54	0.0	0.0
softclip_right	chimeric	12.90	22.12	0.0	19.0
softclip_right	clean	0.21	1.51	0.0	0.0
total_clipped_bases	chimeric	25.44	25.48	19.0	48.0
total_clipped_bases	clean	0.44	2.16	0.0	0.0
kmer_js_divergence	chimeric	0.974	0.025	0.986	0.043
kmer_js_divergence	clean	0.976	0.025	0.986	0.040
kmer_cosine_diff	chimeric	0.974	0.026	0.986	0.042
kmer_cosine_diff	clean	0.976	0.025	0.986	0.041
microhomology_length	chimeric	0.458	0.755	0.0	1.0
microhomology_length	clean	0.462	0.758	0.0	1.0
microhomology_gc	chimeric	0.172	0.361	0.0	0.0
microhomology_gc	clean	0.172	0.361	0.0	0.0

823 Boxplots were generated for each feature, with the x-axis representing the
 824 class (clean reads and chimeric reads) and the y-axis representing the feature
 825 value. Figure 4.1 presents a panel of selected key features, while boxplots for all
 826 numeric features are provided in Appendix B.

827 For clipping-related features (`softclip_left`, `softclip_right`,
 828 and `total_clipped_bases`), chimeric reads exhibit higher medians and longer
 829 upper whiskers than clean reads, indicating increased variability and the presence
 830 of split alignments.

831 Supplementary alignment features (`has_sa` and `sa_count`), show that clean
 832 reads are largely zero, whereas chimeric reads display a wider distribution, re-

833 reflecting frequent supplementary alignments.

834 K-mer metrics (`kmer_js_divergence` and `kmer_cosine_diff`) show a slight
835 upward shift for chimeric reads, but substantial overlap with clean reads indicates
836 low discriminative power.

837 Microhomology features (`microhomology_length` and `microhomology_gc`)
838 have nearly overlapping distributions for both classes, consistent with their low
839 standalone predictive importance.

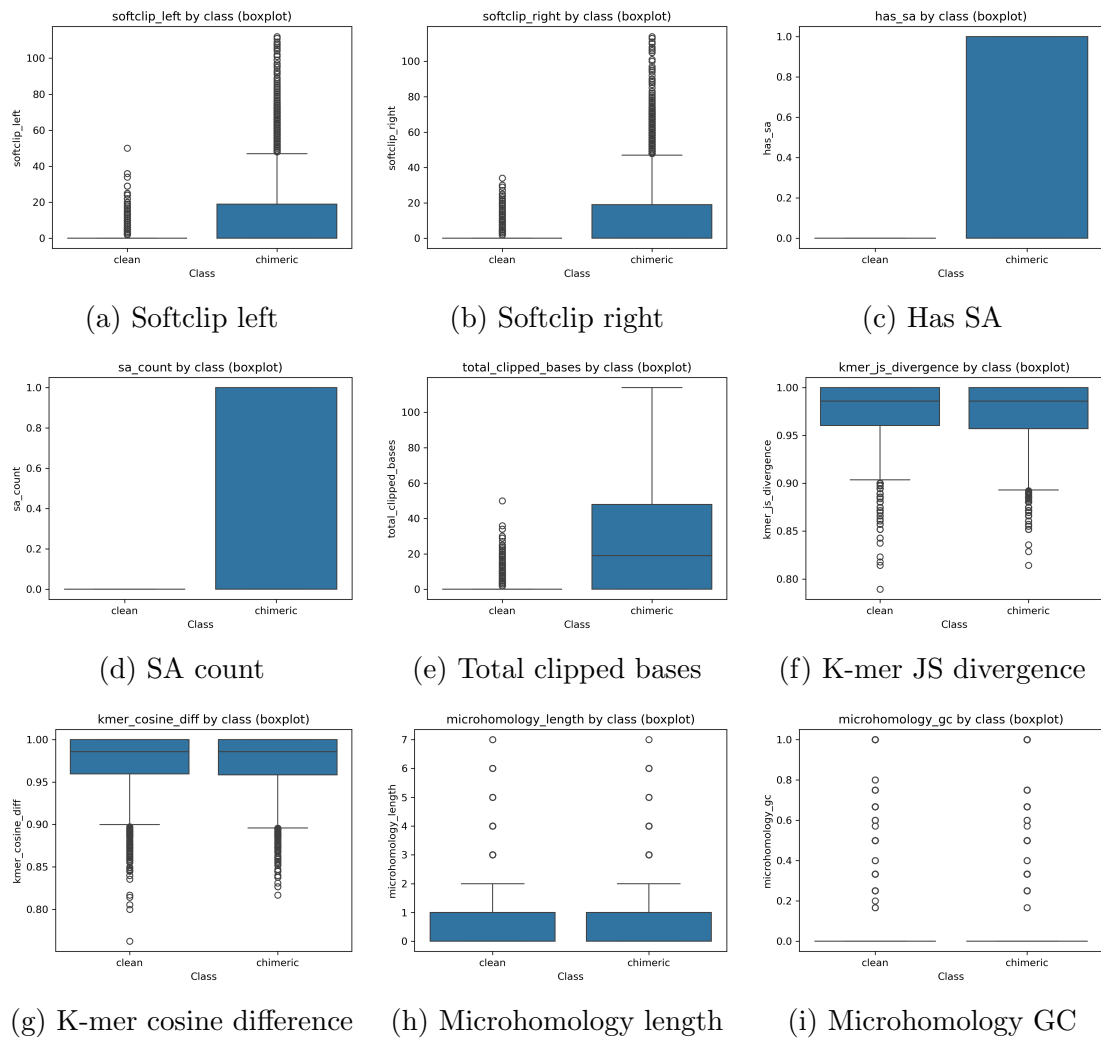


Figure 4.1: Boxplots of selected features for clean and chimeric reads.

840 4.1.2 Correlation Analysis of Extracted Features

841 A feature correlation heatmap (Figure 4.2) was generated to examine relationships
842 among the extracted variables and to identify patterns of redundancy and inde-
843 pendence within the feature set. The analysis shows that alignment-related and
844 clipping-related features form a strongly correlated cluster, including indicators
845 of supplementary alignments, alignment segment counts, positional differences,
846 and soft-clipping measures. These features capture related aspects of alignment
847 fragmentation, which is a known characteristic of chimeric reads, and several
848 show moderate correlations with the class label, supporting their relevance for
849 distinguishing chimeric from clean reads. In contrast, general read-quality and
850 alignment-quality metrics, such as read length, base quality, and mapping qual-
851 ity, exhibit weak correlations with most split-alignment features, indicating that
852 they provide distinct information rather than overlapping with alignment-derived
853 signals. Sequence-based features display a similar pattern of independence, as
854 k-mer divergence metrics show weak correlations with other feature groups, while
855 microhomology features exhibit generally low correlations with both alignment-
856 based and k-mer-based features. Overall, the correlation structure highlights in-
857 tentional redundancy within alignment-derived features and clear separation be-
858 tween feature families, supporting the use of features that capture different aspects
859 of chimeric read characteristics to improve chimera classification.

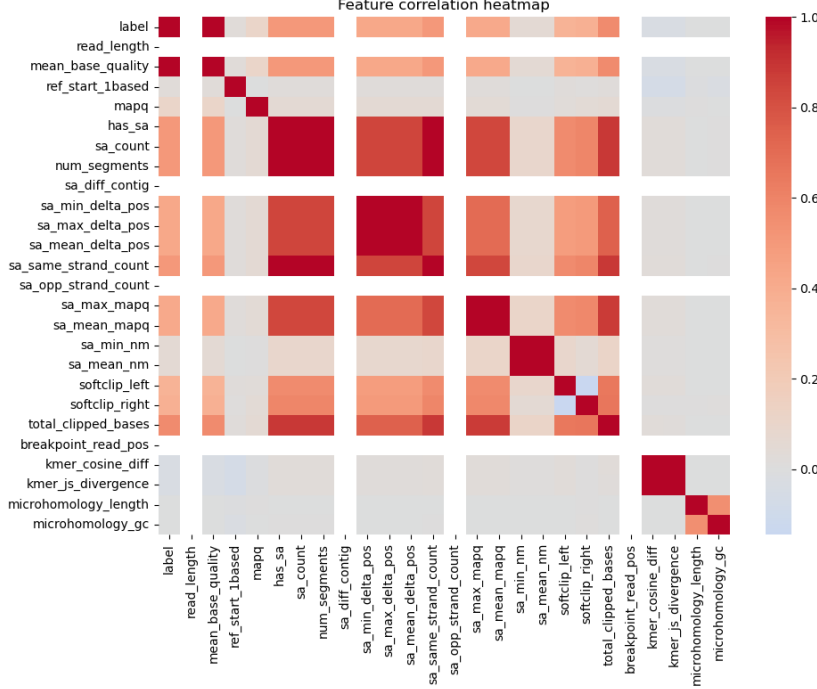


Figure 4.2: Feature correlation heatmap showing relationships among alignment-derived and sequence-derived features.

860 4.2 Baseline Classification Performance

861 Table ?? summarises the performance of thirteen baseline classifiers trained on
 862 the engineered feature set and evaluated on a held-out test set. All models were
 863 trained using default hyperparameters, without dedicated tuning.

864 The dummy baseline, which always predicts the same class regardless of the
 865 input features, achieved a test accuracy of approximately 0.50 and an F1-score of
 866 0.67. This reflects the balanced class distribution and serves as a lower bound for
 867 meaningful model performance.

868 Across the remaining models, test F1-scores clustered within a narrow range,

869 from approximately 0.75 to 0.78, with ROC–AUC values between about 0.82
 870 and 0.85. Ensemble methods, including gradient boosting, CatBoost, LightGBM,
 871 XGBoost, bagging trees, and random forest, exhibited very similar performance.
 872 Among these, CatBoost and gradient boosting achieved the highest scores, with
 873 test F1-scores of approximately 0.775 and ROC–AUC values of approximately
 874 0.84. Linear models, namely logistic regression and the calibrated linear SVM,
 875 performed slightly worse, with test F1-scores around 0.75. In contrast, Gaussian
 876 Naive Bayes lagged behind with a substantially lower F1-score of approximately
 877 0.66, despite exhibiting extremely high precision for the chimeric class.

Table 4.2: Performance of baseline classifiers on the held-out test set.

model	test_accuracy	test_precision	test_recall	test_f1	test_roc_auc
dummy_baseline	0.500188	0.500188	1.000000	0.666833	0.500000
logreg_l2	0.790797	0.945956	0.617000	0.746860	0.829807
linear_svm_calibrated	0.791422	0.947773	0.617000	0.747426	0.829602
random_forest	0.800050	0.910427	0.665750	0.769097	0.832766
extra_trees	0.797924	0.918833	0.653750	0.763950	0.826517
gradient_boosting	0.809053	0.947521	0.654500	0.774213	0.844844
xgboost	0.807303	0.942107	0.655000	0.772747	0.841042
lightgbm	0.806052	0.936231	0.657000	0.772146	0.841671
catboost	0.808803	0.941408	0.658750	0.775114	0.843362
knn	0.789671	0.902990	0.649250	0.755381	0.820898
gaussian_nb	0.745780	0.997975	0.492750	0.659749	0.826918
bagging_trees	0.800550	0.910830	0.666500	0.769742	0.837357
mlp	0.793047	0.949062	0.619500	0.749660	0.829611

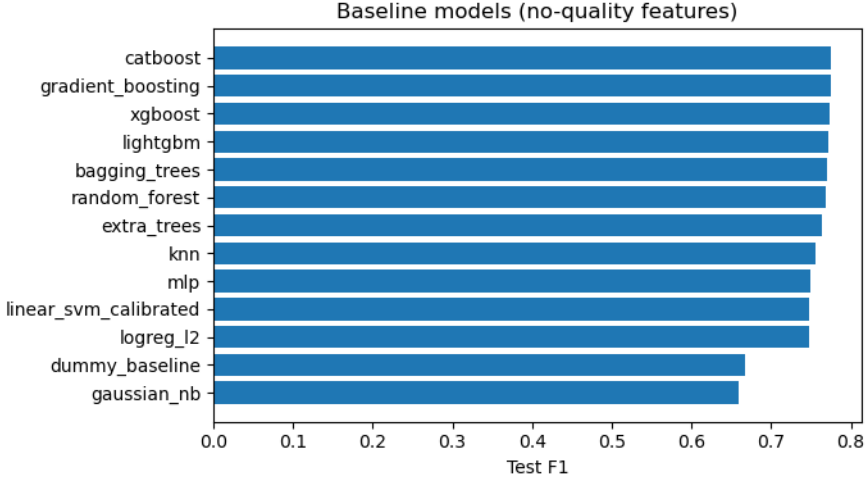


Figure 4.3: Test F1 of all baseline classifiers.

878 4.3 Effect of Hyperparameter Tuning

879 To assess whether performance could be improved further, ten model families un-
 880 derwent randomised hyperparameter search. The tuned metrics are summarised
 881 in Table 4.3. Overall, tuning yielded modest but consistent gains for tree-based en-
 882 sembles and boosting methods, while leaving linear models essentially unchanged
 883 or slightly worse.

884 CatBoost, gradient boosting, LightGBM, random forest, bagging trees, and
 885 extra trees experienced small increases in test F1 after tuning, typically on the
 886 order of $\Delta F1 \approx 0.002\text{--}0.006$, with corresponding improvements in ROC–AUC of
 887 up to approximately $\Delta AUC \approx 0.009$. In contrast, XGBoost and the multilayer
 888 perceptron showed negligible change or slight decreases in F1, while linear models
 889 did not benefit from tuning.

890 After tuning, gradient boosting achieved the best overall test performance,

891 with a test F1-score of 0.776 and a ROC–AUC of 0.846. LightGBM and bagging
 892 trees followed closely, attaining test F1-scores of 0.774 and 0.772 and ROC–AUC
 893 values of 0.843 and 0.842, respectively. Random forest also improved modestly
 894 to a test F1-score of 0.772 with a ROC–AUC of 0.839. CatBoost, with a test
 895 F1-score of 0.775 and ROC–AUC of 0.843, achieved marginal changes relative to
 896 its baseline performance.

Table 4.3: Performance of tuned classifiers on the held-out test set.

model_name	test_f1_base	test_roc_auc_base	test_f1_tuned	test_roc_auc_tuned
gradient_boosting	0.774213	0.844844	0.776460	0.845858
catboost	0.775114	0.843362	0.775289	0.842918
lightgbm	0.772146	0.841671	0.773802	0.843451
bagging_trees	0.769742	0.837357	0.772422	0.841870
random_forest	0.769097	0.832766	0.772376	0.838799
xgboost	0.772747	0.841042	0.770118	0.843225
extra_trees	0.763950	0.826517	0.769878	0.834912
mlp	0.749660	0.829611	0.749167	0.828506
logreg_l2	0.746860	0.829807	0.745187	0.825632
linear_svm_calibrated	0.747426	0.829602	0.744848	0.825147

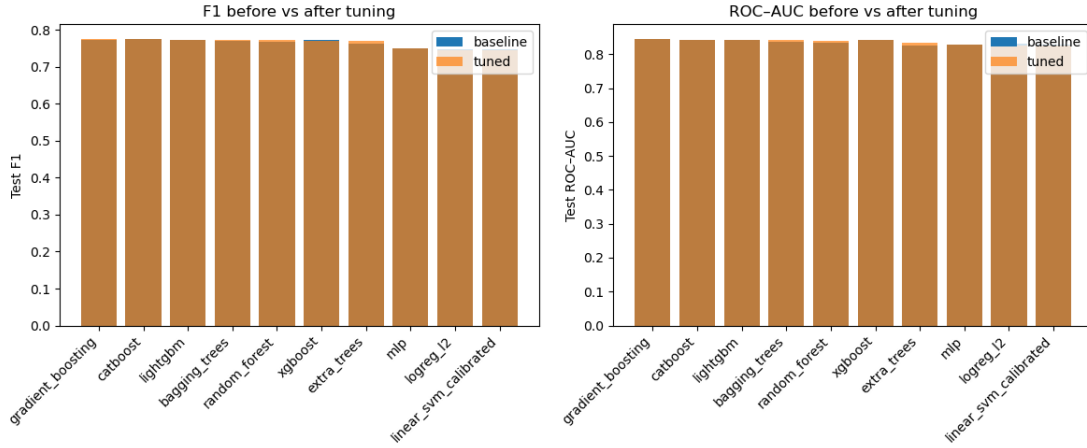


Figure 4.4: Comparison of test F1 (left) and ROC–AUC (right) for baseline and tuned models.

897 Because improvements are small and within cross-validation variability, tun-

898 ing was interpreted as stabilising and slightly refining the models rather than
899 completely altering their behaviour or their relative ranking.

900 **4.4 Detailed Evaluation of Representative Mod-**
901 **els**

902 For interpretability and diversity, four tuned models were selected for deeper
903 analysis: CatBoost (best-performing boosted tree), scikit-learn gradient boost-
904 ing (canonical gradient-boosting implementation), random forest (non-boosted
905 ensemble baseline), and L_2 -regularised logistic regression (linear baseline). All
906 models were trained on the engineered feature set and evaluated on the same
907 held-out test data.

908 **4.4.1 Confusion Matrices and Error Patterns**

909 Classification reports and confusion matrices for the four models reveal consistent
910 patterns. CatBoost and gradient boosting both achieved overall accuracy around
911 0.81, with similar macro-averaged F1 scores (0.80–0.805). For CatBoost, precision
912 and recall for clean reads were 0.74 and 0.95, respectively, while for chimeric
913 reads they were 0.94 and 0.66 ($F1 = 0.775$). Gradient boosting showed nearly
914 identical trade-offs, with clean read precision/recall of 0.74/0.96 and chimeric
915 read precision/recall of 0.94/0.66 ($F1 = 0.777$).

916 Bagging trees achieved slightly lower accuracy (0.805) and chimeric F1 (0.772),
917 whereas the multilayer perceptron (MLP) attained the lowest accuracy (0.793) and

918 chimeric F1 (0.749), despite achieving high chimeric precision (0.95) at the cost
919 of lower recall (0.62).

920 Across all models, errors were asymmetric: false negatives (chimeric reads
921 predicted as clean) were more frequent than false positives. For instance, CatBoost
922 misclassified 1,352 chimeric reads as clean but only 215 clean reads as chimeric,
923 while gradient boosting misclassified 1,352 chimeric reads as clean and 181 clean
924 reads as chimeric. This pattern indicates that both models are conservative,
925 prioritizing the avoidance of false chimera calls even if some true chimeras are
926 missed. Consultation with PGC Visayas suggested that this conservative behavior
927 is generally acceptable, although further evaluation is needed to assess its impact
928 on downstream analyses.

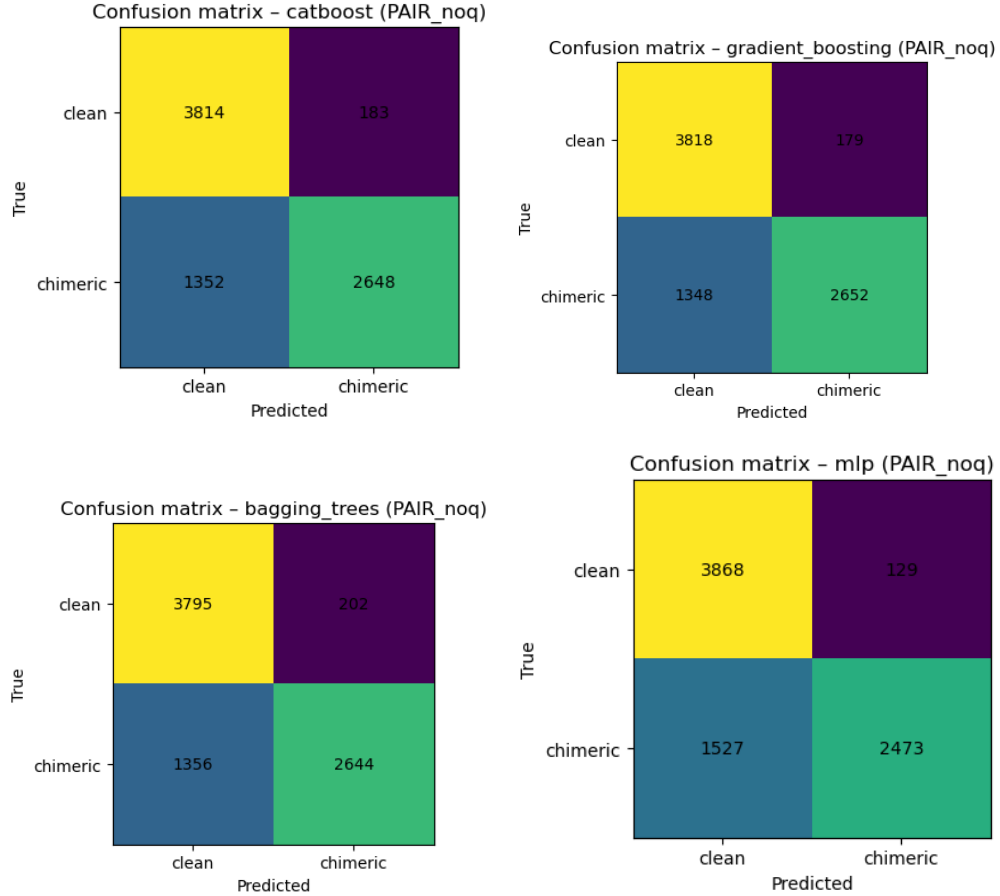


Figure 4.5: Confusion matrices for the four representative models on the held-out test set.

929 4.4.2 ROC and Precision–Recall Curves

930 Receiver operating characteristic (ROC) and precision–recall (PR) curves as
931 shown in Figure 4.6 further support the similarity among the top models. The
932 three tree-based ensembles (CatBoost, gradient boosting, bagging trees) achieved
933 ROC–AUC values of approximately 0.84 and average precision (AP) around 0.88.
934 MLP performed slightly worse (AUC \approx 0.82, AP \approx 0.87) but still substantially
935 better than the dummy baseline.

936 The PR curves show that precision remains above 0.9 across a broad range
 937 of recall values (up to roughly 0.5–0.6), after which precision gradually declines.
 938 This behaviour indicates that the models can assign very high confidence to a
 939 subset of chimeric reads, while more ambiguous reads can only be recovered by
 940 accepting lower precision.

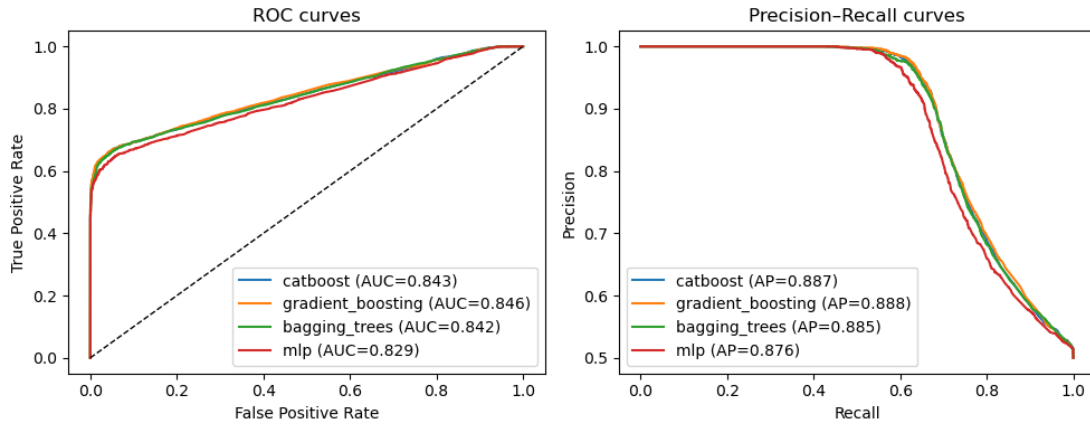


Figure 4.6: ROC (left) and precision–recall (right) curves for the four representative models on the held-out test set.

941 4.5 Feature Importance

942 4.5.1 Permutation Importance of Individual Features

943 To understand how each classifier made predictions, feature importance was quan-
 944 tified using permutation importance. This analysis was applied to four represen-
 945 tative models: CatBoost, Gradient Boosting, Bagging Trees, and an MLP.

946 As shown in Figure 4.7, `total_clipped_bases` consistently provides a
 947 strong predictive signal across all models, particularly in Gradient Boost-

948 ing (importance = 0.117) and Bagging Trees (importance = 0.274). Cat-
949 Boost assigns high importance to both `total_clipped_bases` (0.062) and
950 `kmer_js_divergence` (0.045), while MLP relies on `total_clipped_bases` and
951 soft-clipping features (`softclip_left`, `softclip_right`) as primary signals. Gra-
952 dient Boosting emphasizes `kmer_js_divergence` and `kmer_cosine_diff` alongside
953 `total_clipped_bases`, but soft-clipping features contribute less.

954 Microhomology features (`microhomology_length` and `microhomology_gc`)
955 provide minimal predictive value in all models, and some alignment-based split-
956 read metrics (e.g., `sa_min_delta_pos`, `sa_max_delta_pos`) are leveraged primarily
957 by the MLP. Overall, these results indicate that accurate detection of chimeric
958 reads relies on both alignment-based signals and k-mer compositional information,
959 with explicit microhomology features contributing little. Combining multiple
960 feature types enhances model sensitivity and specificity.

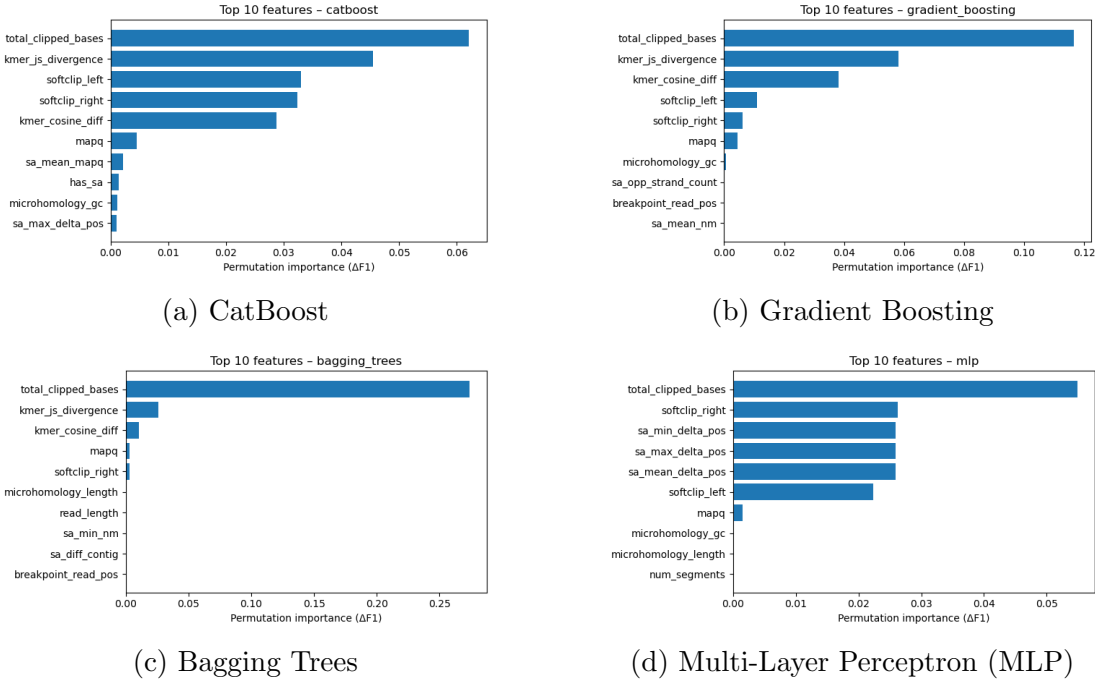


Figure 4.7: Permutation-based feature importance for four representative classifiers.

961 4.5.2 Feature Family Importance

962 To evaluate broader predictive signals, features were grouped into five fam-
 963 ilies: SA_structure (supplementary alignment and segment metrics, e.g.,
 964 has_sa, sa_count, sa_min_delta_pos, sa_mean_nm), Clipping (softclip_left,
 965 softclip_right, total_clipped_bases, breakpoint_read_pos), Kmer_jump
 966 (kmer_cosine_diff, kmer_js_divergence), Micro_homology (microhomology_length,
 967 microhomology_gc), and Other (e.g., mapq).

968 Aggregated analyses reveal consistent patterns across models. In CatBoost,
 969 the Clipping family dominates with cumulative importance 0.127, followed
 970 by Kmer_jump (0.074), while Other (0.0045), SA_structure (0.0033), and Mi-

971 cro_homology (0.0013) contribute minimally. Gradient Boosting shows a similar
972 trend, with Clipping (0.134) and Kmer_jump (0.096) providing most predictive
973 power, and the remaining families contributing negligibly. Bagging Trees empha-
974 sizes Clipping even more strongly (0.277), with Kmer_jump secondary (0.037),
975 and SA_structure, Micro_homology, and Other remaining minor contributors.
976 Interestingly, the MLP exhibits a different pattern, prioritizing Clipping (0.104)
977 and SA_structure (0.078), while Kmer_jump (0.000034) and Micro_homology
978 (0.000091) have almost no effect.

979 Both feature-level and aggregated analyses indicate that accurate detection
980 of chimeric reads in this dataset relies primarily on alignment irregularities cap-
981 tured by Clipping features and, in most tree-based models, on k-mer composi-
982 tional shifts (Kmer_jump), which often arise from PCR-induced template switch-
983 ing events. Explicit microhomology features contribute minimally, and some re-
984 liance on SA_structure signals is observed only in the MLP.

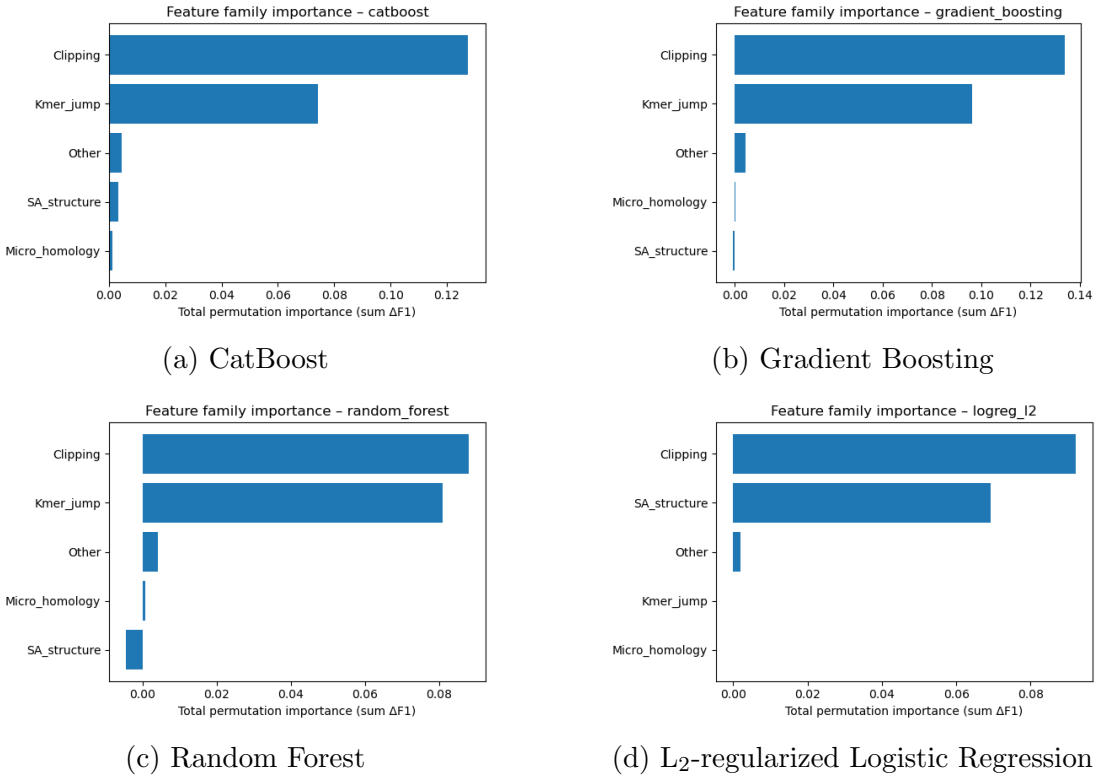


Figure 4.8: Aggregated feature family importance across four models.

985 4.6 Feature Selection

986 Feature selection was performed to identify the smallest subset reaching 95% cu-
 987 mulative importance. Three models were evaluated as references: the full model
 988 with all 23 features, a reduced model with the top- k features, and an ablation
 989 model excluding microhomology features, using a tuned CatBoost classifier to
 990 assess feature contributions and overall classification performance.

`991` 4.6.1 Cumulative Importance Curve

`992` The cumulative importance curve was computed using the tuned Gradient Boost-
`993` ing classifier. Figure 4.9 illustrates the contribution of features sorted by impor-
`994` tance. The curve rises steeply for the top features and then gradually plateaus,
`995` indicating that a small number of features capture most of the model’s pre-
`996` dictive power. A cumulative importance of 95% is reached at $k = 4$ features,
`997` which are `total_clipped_bases`, `kmer_js_divergence`, `kmer_cosine_diff`, and
`998` `softclip_left`.

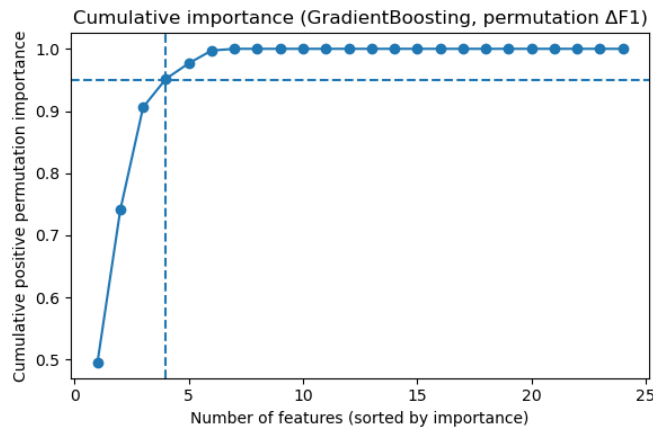


Figure 4.9: Cumulative importance curve of features sorted by importance.

`999` 4.6.2 Performance Comparison Across Feature Sets

`1000` Classification performance was compared across three feature sets using a tuned
`1001` Gradient Boosting classifier. The full model, incorporating all 24 engineered fea-
`1002` tures, achieved an F1 score of 0.7765 and a ROC–AUC of 0.8459. A reduced model
`1003` using only the top four features (`total_clipped_bases`, `kmer_js_divergence`,
`1004` `kmer_cosine_diff`, and `softclip_left`) achieved nearly equivalent performance

1005 with an F1 of 0.7768 and a ROC–AUC of 0.8369. An ablation model excluding mi-
 1006 crohomology features (`microhomology_length` and `microhomology_gc`) also per-
 1007 formed comparably, with an F1 of 0.7761 and ROC–AUC of 0.8444. These results
 1008 indicate that clipping and k-mer features capture almost all predictive signal,
 1009 while microhomology features are largely redundant in this dataset.

Table 4.4: Test set performance of three feature set variants using tuned Gradient Boosting.

Variant	No. of Features	Test F1	ROC–AUC
Full Gradient Boost	24	0.7765	0.8459
Selected (top-4)	4	0.7768	0.8369
No microhomology	22	0.7761	0.8444

1010 Figure 4.10 presents a bar chart comparing F1 and ROC–AUC across the
 1011 three variants, with the x-axis showing the model variants and two bars per group
 1012 representing the F1 and ROC–AUC values.

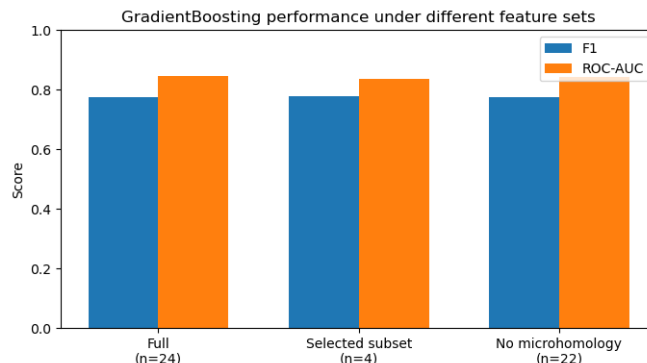


Figure 4.10: Comparison of F1 and ROC–AUC for the full, top-4 selected, and no-microhomology feature set variants.

1013 **4.6.3 Interpretation and Final Feature Set Choice**

1014 The full 23-feature model is retained as the primary configuration for the re-
1015 mainder of the study, while the four-feature subset serves as a lightweight al-
1016 ternative. Clipping features reflect alignment junctions and mapping disruptions
1017 typical of chimeric reads, and k-mer divergence captures changes in sequence com-
1018 position across breakpoints. Microhomology features appear largely redundant,
1019 as their signal is either indirectly represented by clipping and k-mer features or
1020 not strongly expressed in the simulation dataset.

1021 **4.7 Summary of Findings**

1022 All evaluated machine learning models substantially outperformed the dummy
1023 baseline, demonstrating that the engineered feature set contains meaningful
1024 signals for detecting PCR-induced chimeric reads. Across classifiers, the best-
1025 performing models achieved test F1-scores of approximately 0.77 and ROC–AUC
1026 values around 0.84 on held-out simulated mitochondrial reads, indicating reli-
1027 able discrimination between clean and chimeric sequences. Among the tested
1028 approaches, tree-based ensemble and boosting methods consistently showed the
1029 strongest and most stable performance. In particular, CatBoost and Gradient
1030 Boosting ranked among the top models across multiple evaluation metrics,
1031 both before and after hyperparameter tuning. These results suggest that non-
1032 linear ensemble methods are well suited to capturing the interaction between
1033 alignment-derived and sequence-derived features in this setting.

1034 Analysis of feature behaviour revealed clear differences in how effectively fea-

ture groups distinguished clean and chimeric reads. Alignment- and clipping-based features, such as soft-clipping measures and total clipped bases, showed strong separation between clean and chimeric reads and emerged as the most informative signals. K-mer divergence features provided additional but weaker separation, contributing complementary information beyond alignment irregularities. In contrast, microhomology features and several supplementary alignment (SA) structure metrics exhibited minimal class separation and contributed little to overall predictive performance.

Feature selection results further supported these observations. A reduced subset of four features, dominated by clipping-based and k-mer divergence metrics, achieved nearly identical performance to the full 23-feature model. Moreover, removing explicit microhomology features did not degrade performance and in some cases resulted in slightly improved metrics, suggesting that these features are largely redundant under the simulated conditions tested.

Overall, these findings suggest that alignment-based and k-mer-based features provide sufficient signal to detect PCR-induced chimeric reads in simulated mitochondrial data, supporting the use of a compact and interpretable machine learning approach as a pre-assembly chimera detection step.

1053 **Appendix A**

1054 **Complete Per-Class Summary**

1055 **Statistics**

Table A.1: Complete per-class summary statistics for all extracted features.

Feature	Class	Mean	Std	Median	Q1	Q3	IQR	Min	Max	n
breakpoint_read_pos	chimeric	75.000	0.000	75.000	75.000	75.000	0.000	75.000	75.000	20000
breakpoint_read_pos	clean	75.000	0.000	75.000	75.000	75.000	0.000	75.000	75.000	19983
has_sa	chimeric	0.406	0.491	0.000	0.000	1.000	1.000	0.000	1.000	20000
has_sa	clean	0.000	0.000	0.000	0.000	0.000	0.000	0.000	0.000	19983
kmer_cosine_diff	chimeric	0.974	0.026	0.986	0.958	1.000	0.042	0.817	1.000	20000
kmer_cosine_diff	clean	0.976	0.025	0.986	0.959	1.000	0.041	0.814	1.000	19983
kmer_js_divergence	chimeric	0.974	0.025	0.986	0.957	1.000	0.043	0.811	1.000	20000
kmer_js_divergence	clean	0.976	0.025	0.986	0.959	1.000	0.040	0.817	1.000	19983
mapq	chimeric	59.987	0.355	60.000	60.000	60.000	0.000	43.000	60.000	20000
mapq	clean	59.663	2.036	60.000	60.000	60.000	0.000	0.000	60.000	19983
mean_base_quality	chimeric	40.000	0.000	40.000	40.000	40.000	0.000	40.000	40.000	20000
mean_base_quality	clean	13.000	0.000	13.000	13.000	13.000	0.000	13.000	13.000	19983
microhomology_gc	chimeric	0.172	0.361	0.000	0.000	0.000	0.000	0.000	1.000	20000
microhomology_gc	clean	0.172	0.361	0.000	0.000	0.000	0.000	0.000	1.000	19983
microhomology_length	chimeric	0.458	0.755	0.000	0.000	1.000	1.000	0.000	5.000	20000
microhomology_length	clean	0.462	0.758	0.000	0.000	1.000	1.000	0.000	5.000	19983

Continued on next page

Feature	Class	Mean	Std	Median	Q1	Q3	IQR	Min	Max	n
num_segments	chimeric	1.406	0.491	1.000	1.000	2.000	1.000	1.000	2.000	20000
num_segments	clean	1.000	0.000	1.000	1.000	1.000	0.000	1.000	1.000	19983
read_length	chimeric	150.000	0.000	150.000	150.000	150.000	0.000	150.000	150.000	20000
read_length	clean	150.000	0.000	150.000	150.000	150.000	0.000	150.000	150.000	19983
ref_start_1based	chimeric	8428.635	4248.348	8433.000	5013.000	11786.250	6773.250	1.000	16521.000	20000
ref_start_1based	clean	8200.121	4626.918	8240.000	3639.000	11565.000	7926.000	1.000	16521.000	19983
sa_count	chimeric	0.406	0.491	0.000	0.000	1.000	1.000	0.000	1.000	20000
sa_count	clean	0.000	0.000	0.000	0.000	0.000	0.000	0.000	0.000	19983
sa_diff_contig	chimeric	0.000	0.000	0.000	0.000	0.000	0.000	0.000	0.000	20000
sa_diff_contig	clean	0.000	0.000	0.000	0.000	0.000	0.000	0.000	0.000	19983
sa_max_delta_pos	chimeric	1573.531	2364.996	0.000	0.000	2826.250	2826.250	0.000	16519.000	20000
sa_max_delta_pos	clean	0.000	0.000	0.000	0.000	0.000	0.000	0.000	0.000	19983
sa_max_mapq	chimeric	14.104	21.424	0.000	0.000	27.000	27.000	0.000	60.000	20000
sa_max_mapq	clean	0.000	0.000	0.000	0.000	0.000	0.000	0.000	0.000	19983
sa_mean_delta_pos	chimeric	1573.531	2364.996	0.000	0.000	2826.250	2826.250	0.000	16519.000	20000
sa_mean_delta_pos	clean	0.000	0.000	0.000	0.000	0.000	0.000	0.000	0.000	19983
sa_mean_mapq	chimeric	14.104	21.424	0.000	0.000	27.000	27.000	0.000	60.000	20000
sa_mean_mapq	clean	0.000	0.000	0.000	0.000	0.000	0.000	0.000	0.000	19983

Continued on next page

Feature	Class	Mean	Std	Median	Q1	Q3	IQR	Min	Max	n
sa_mean_nm	chimeric	0.022	0.319	0.000	0.000	0.000	0.000	0.000	6.000	20000
sa_mean_nm	clean	0.000	0.000	0.000	0.000	0.000	0.000	0.000	0.000	19983
sa_min_delta_pos	chimeric	1573.531	2364.996	0.000	0.000	2826.250	2826.250	0.000	16519.000	20000
sa_min_delta_pos	clean	0.000	0.000	0.000	0.000	0.000	0.000	0.000	0.000	19983
sa_min_nm	chimeric	0.022	0.319	0.000	0.000	0.000	0.000	0.000	6.000	20000
sa_min_nm	clean	0.000	0.000	0.000	0.000	0.000	0.000	0.000	0.000	19983
sa_opp_strand_count	chimeric	0.000	0.000	0.000	0.000	0.000	0.000	0.000	0.000	20000
sa_opp_strand_count	clean	0.000	0.000	0.000	0.000	0.000	0.000	0.000	0.000	19983
sa_same_strand_count	chimeric	0.406	0.491	0.000	0.000	1.000	1.000	0.000	1.000	20000
sa_same_strand_count	clean	0.000	0.000	0.000	0.000	0.000	0.000	0.000	0.000	19983
softclip_left	chimeric	12.546	21.898	0.000	0.000	19.000	19.000	0.000	150.000	20000
softclip_left	clean	0.225	1.543	0.000	0.000	0.000	0.000	0.000	56.000	19983
softclip_right	chimeric	12.896	22.123	0.000	0.000	19.000	19.000	0.000	150.000	20000
softclip_right	clean	0.212	1.513	0.000	0.000	0.000	0.000	0.000	55.000	19983
total_clipped_bases	chimeric	25.442	25.481	19.000	0.000	48.000	48.000	0.000	150.000	20000
total_clipped_bases	clean	0.437	2.157	0.000	0.000	0.000	0.000	0.000	110.000	19983

1057 **Appendix B**

1058 **Boxplots for All Numeric**

1059 **Features by Feature Family**

1060 **B.0.1 SA Structure (Supplementary Alignment and Seg-**
1061 **ment Metrics)**

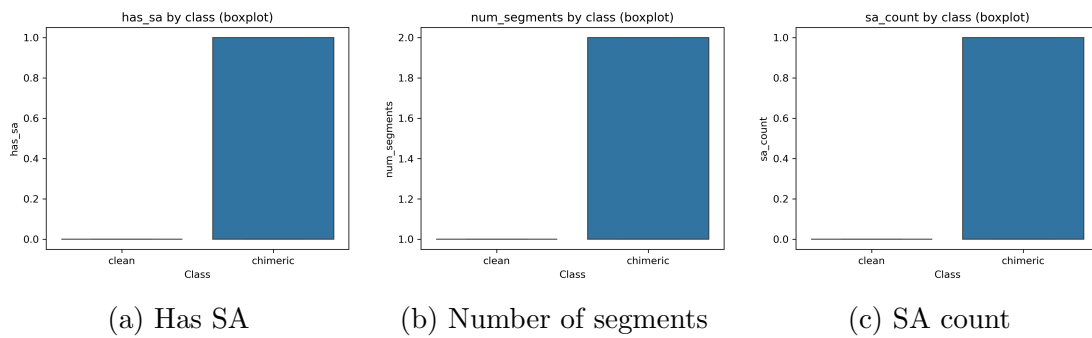


Figure B.1: Boxplots of SA Structure features by class (1/2).

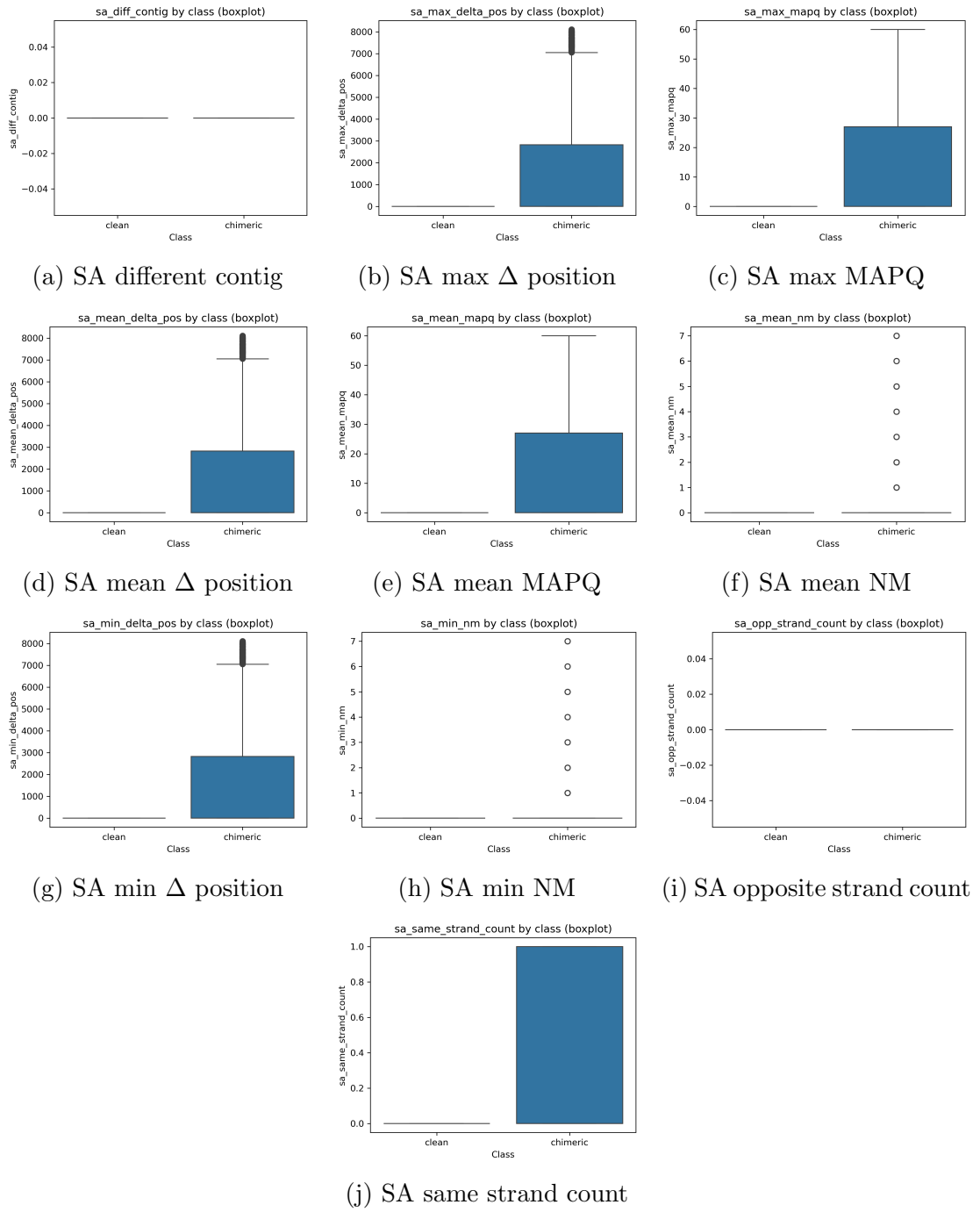


Figure B.2: Boxplots of SA Structure features by class (2/2).

1062 **B.0.2 Clipping-Based Features**

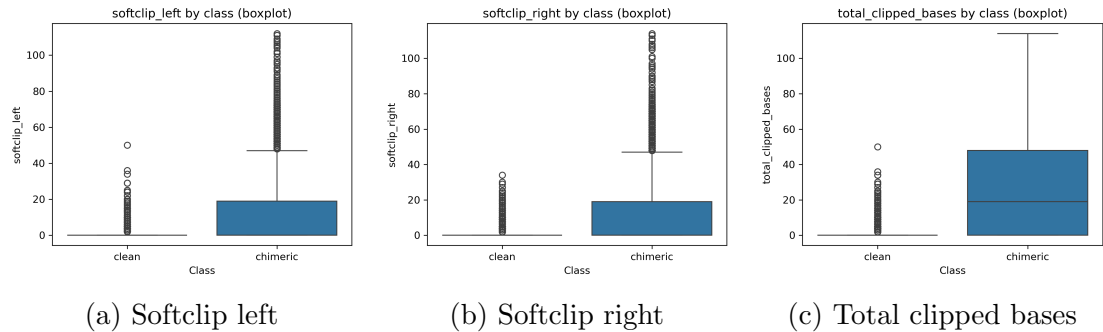


Figure B.3: Boxplots of clipping-based features by class.

1063 **B.0.3 K-mer Features**



Figure B.4: Boxplots of k-mer features by class.

1064 **B.0.4 Microhomology Features**



Figure B.5: Boxplots of microhomology features by class.

1065 **B.0.5 Others**

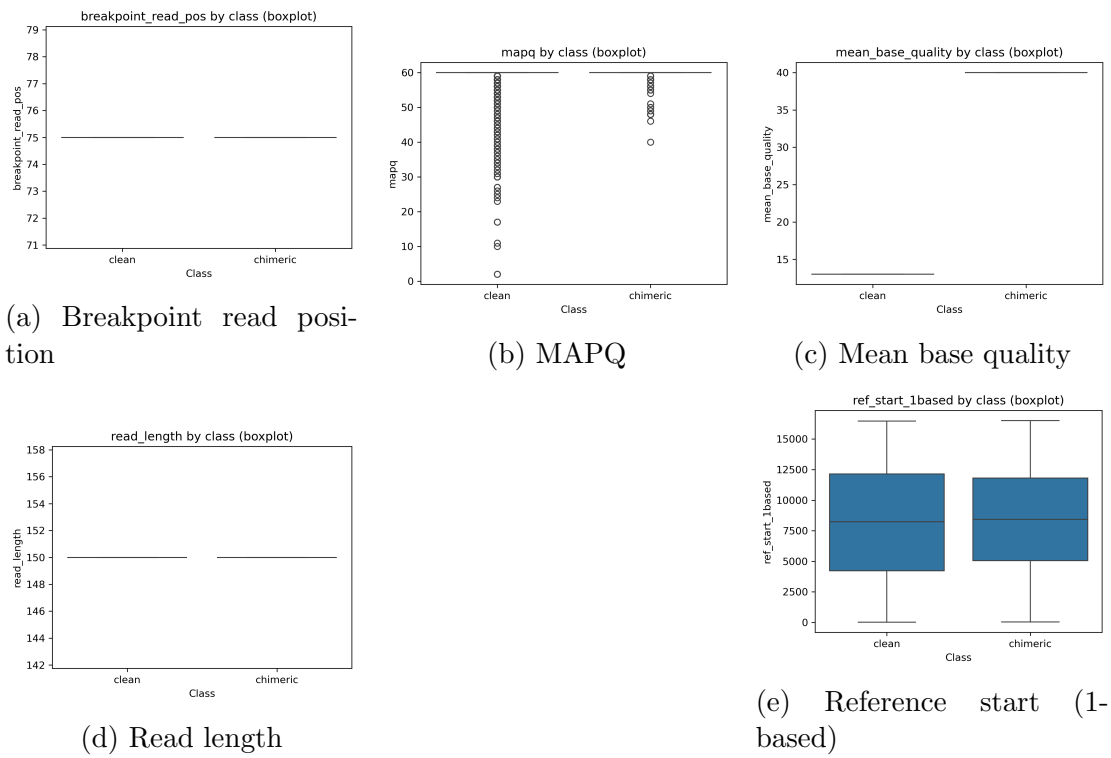


Figure B.6: Boxplots of other numeric features by class.

¹⁰⁶⁶ References

- ¹⁰⁶⁷ Anderson, S., Bankier, A., Barrell, B., Bruijn, M., Coulson, A., Drouin, J., ...
¹⁰⁶⁸ Young, I. (1981, 04). Sequence and organization of the human mitochondrial
¹⁰⁶⁹ genome. *Nature*, *290*, 457-465. doi: 10.1038/290457a0
- ¹⁰⁷⁰ Arango, G., Garner, E., Pruden, A., Heath, L., Vikesland, P., & Zhang, L. (2018,
¹⁰⁷¹ 02). Deeparg: A deep learning approach for predicting antibiotic resistance
¹⁰⁷² genes from metagenomic data. *Microbiome*, *6*. doi: 10.1186/s40168-018
¹⁰⁷³ -0401-z
- ¹⁰⁷⁴ Bentley, D. R., Balasubramanian, S., Swerdlow, H. P., Smith, G. P., Milton, J.,
¹⁰⁷⁵ Brown, C. G., ... Smith, A. J. (2008). Accurate whole human genome
¹⁰⁷⁶ sequencing using reversible terminator chemistry. *Nature*, *456*(7218), 53–
¹⁰⁷⁷ 59. doi: 10.1038/nature07517
- ¹⁰⁷⁸ Boore, J. L. (1999). Animal mitochondrial genomes. *Nucleic Acids Research*,
¹⁰⁷⁹ *27*(8), 1767–1780. doi: 10.1093/nar/27.8.1767
- ¹⁰⁸⁰ Cameron, S. L. (2014). Insect mitochondrial genomics: Implications for evolution
¹⁰⁸¹ and phylogeny. *Annual Review of Entomology*, *59*, 95–117. doi: 10.1146/
¹⁰⁸² annurev-ento-011613-162007
- ¹⁰⁸³ Dierckxsens, N., Mardulyn, P., & Smits, G. (2017). Novoplasty: de novo assembly
¹⁰⁸⁴ of organelle genomes from whole genome data. *Nucleic Acids Research*,

- 1085 45(4), e18. doi: 10.1093/nar/gkw955
- 1086 Edgar, R. C. (n.d.). *Uchime in practice*. Retrieved from https://www.drive5.com/usearch/manual7/uchime_practical.html
- 1088 Edgar, R. C. (2016). Uchime2: improved chimera prediction for amplicon se-
1089 quencing. *bioRxiv*. Retrieved from <https://api.semanticscholar.org/>
1090 CorpusID:88955007
- 1091 Edgar, R. C., Haas, B. J., Clemente, J. C., Quince, C., & Knight, R. (2011).
1092 Uchime improves sensitivity and speed of chimera detection. *Bioinformatics*,
1093 27(16), 2194–2200. doi: 10.1093/bioinformatics/btr381
- 1094 Glenn, T. C. (2011). Field guide to next-generation dna sequencers. *Molecular
1095 Ecology Resources*, 11(5), 759–769. doi: 10.1111/j.1755-0998.2011.03024.x
- 1096 Gonzalez, J. M., Zimmermann, J., & Saiz-Jimenez, C. (2004, 09). Evalu-
1097 ating putative chimeric sequences from pcr-amplified products. *Bioin-
1098 formatics*, 21(3), 333-337. Retrieved from <https://doi.org/10.1093/bioinformatics/bti008>
1099 doi: 10.1093/bioinformatics/bti008
- 1100 Gray, M. W. (2012). Mitochondrial evolution. *Cold Spring Harbor perspectives
1101 in biology*, 4. Retrieved from <https://doi.org/10.1101/cshperspect.a011403>
1102 doi: 10.1101/cshperspect.a011403
- 1103 Hahn, C., Bachmann, L., & Chevreux, B. (2013). Reconstructing mitochondrial
1104 genomes directly from genomic next-generation sequencing reads—a baiting
1105 and iterative mapping approach. *Nucleic Acids Research*, 41(13), e129. doi:
1106 10.1093/nar/gkt371
- 1107 Jin, J.-J., Yu, W.-B., Yang, J., Song, Y., dePamphilis, C. W., Yi, T.-S., & Li,
1108 D.-Z. (2020). Getorganelle: a fast and versatile toolkit for accurate de
1109 novo assembly of organelle genomes. *Genome Biology*, 21(1), 241. doi:
1110 10.1186/s13059-020-02154-5

- 1111 Judo, M. S. B., Wedel, W. R., & Wilson, B. H. (1998). Stimulation and sup-
1112 pression of pcr-mediated recombination. *Nucleic Acids Research*, *26*(7),
1113 1819–1825. doi: 10.1093/nar/26.7.1819
- 1114 Labrador, K., Agmata, A., Palermo, J. D., Ravago-Gotanco, R., & Pante, M. J.
1115 (2021). Mitochondrial dna reveals genetically structured haplogroups of
1116 bali sardinella (sardinella lemuru) in philippine waters. *Regional Studies in*
1117 *Marine Science*, *41*, 101588. doi: 10.1016/j.rsma.2020.101588
- 1118 Li, H. (2018, 05). Minimap2: pairwise alignment for nucleotide sequences. *Bioin-*
1119 *formatics*, *34*(18), 3094-3100. Retrieved from <https://doi.org/10.1093/bioinformatics/bty191>
1120 doi: 10.1093/bioinformatics/bty191
- 1121 Liang, Q., Bible, P. W., Liu, Y., Zou, B., & Wei, L. (2020, 02). Deepmi-
1122 crobes: taxonomic classification for metagenomics with deep learning. *NAR*
1123 *Genomics and Bioinformatics*, *2*(1), lqaa009. Retrieved from <https://doi.org/10.1093/nargab/lqaa009> doi: 10.1093/nargab/lqaa009
- 1125 Metzker, M. L. (2010). Sequencing technologies — the next generation. *Nature*
1126 *Reviews Genetics*, *11*(1), 31–46. doi: 10.1038/nrg2626
- 1127 Mysara, M., Saeys, Y., Leys, N., Raes, J., & Monsieurs, P. (2015). Catch,
1128 an ensemble classifier for chimera detection in 16s rrna sequencing stud-
1129 ies. *Applied and Environmental Microbiology*, *81*(5), 1573-1584. Retrieved
1130 from <https://journals.asm.org/doi/abs/10.1128/aem.02896-14> doi:
1131 10.1128/AEM.02896-14
- 1132 Peccoud, J., Lequime, S., Moltini-Conclois, I., Giraud, I., Lambrechts, L., &
1133 Gilbert, C. (2018, 04). A survey of virus recombination uncovers canon-
1134 ical features of artificial chimeras generated during deep sequencing li-
1135 brary preparation. *G3 Genes—Genomes—Genetics*, *8*(4), 1129-1138. Re-
1136 trieved from <https://doi.org/10.1534/g3.117.300468> doi: 10.1534/

- 1137 g3.117.300468
- 1138 Qin, Y., Wu, L., Zhang, Q., Wen, C., Nostrand, J. D. V., Ning, D., ... Zhou, J.
1139 (2023). Effects of error, chimera, bias, and gc content on the accuracy of
1140 amplicon sequencing. *mSystems*, 8(6), e01025-23. Retrieved from <https://journals.asm.org/doi/abs/10.1128/msystems.01025-23> doi: 10.1128/
1141 msystems.01025-23
- 1142
- 1143 Qiu, X., Wu, L., Huang, H., McDonel, P. E., Palumbo, A. V., Tiedje, J. M., &
1144 Zhou, J. (2001). Evaluation of pcr-generated chimeras, mutations, and het-
1145 eroduplexes with 16s rrna gene-based cloning. *Applied and Environmental
1146 Microbiology*, 67(2), 880–887. doi: 10.1128/AEM.67.2.880-887.2001
- 1147 Ren, J., Song, K., Deng, C., Ahlgren, N., Fuhrman, J., Li, Y., ... Sun, F. (2020,
1148 01). Identifying viruses from metagenomic data using deep learning. *Quan-
1149 titative Biology*, 8. doi: 10.1007/s40484-019-0187-4
- 1150 Rodriguez-Martin, B., Palumbo, E., Marco-Sola, S., Griebel, T., Ribeca, P.,
1151 Alonso, G., ... Djebali, S. (2017, 01). Chimpipe: Accurate detection of
1152 fusion genes and transcription-induced chimeras from rna-seq data. *BMC
1153 Genomics*, 18. doi: 10.1186/s12864-016-3404-9
- 1154 Rognes, T., Flouri, T., Nichols, B., Quince, C., & Mahé, F. (2016). Vsearch: a
1155 versatile open source tool for metagenomics. *PeerJ*, 4, e2584. doi: 10.7717/
1156 peerj.2584
- 1157 Sedlazeck, F., Rescheneder, P., Smolka, M., Fang, H., Nattestad, M., von Haeseler,
1158 A., & Schatz, M. (2018, 06). Accurate detection of complex structural
1159 variations using single-molecule sequencing. *Nature Methods*, 15. doi: 10
1160 .1038/s41592-018-0001-7
- 1161 Sfeir, A., & Symington, L. S. (2015). Microhomology-mediated end joining: A
1162 back-up survival mechanism or dedicated pathway? *Trends in Biochemical*

- 1163 *Sciences*, 40(11), 701-714. Retrieved from <https://www.sciencedirect.com/science/article/pii/S0968000415001589> doi: <https://doi.org/10.1016/j.tibs.2015.08.006>
- 1164
- 1165
- 1166 Vervier, K., Mahé, P., Tournoud, M., Veyrieras, J.-B., & Vert, J.-P. (2015,
1167 11). Large-scale machine learning for metagenomics sequence classifica-
1168 tion. *Bioinformatics*, 32(7), 1023-1032. Retrieved from <https://doi.org/10.1093/bioinformatics/btv683> doi: 10.1093/bioinformatics/btv683
- 1169
- 1170 Willette, D., Bognot, E., Mutia, M. T., & Santos, M. (2011). *Biology and ecology
1171 of sardines in the philippines: A review* (Vol. 13; Tech. Rep. No. 1). NFRDI
1172 Technical Paper Series. Retrieved from <https://nfrdi.da.gov.ph/tpjf/etc/Willette%20et%20al.%20Sardines%20Review.pdf>
- 1173